Measurement of the Production Asymmetry between D^0 and $\bar{D}^0$ mesons with proton-proton collisions during Run 2 at the LHCb Experiment

Laxman Seelan
Student ID: 10717429
Department of Physics and Astronomy
The University of Manchester

Performed in collaboration with Samuel Taylor
Supervised by Dr Evelina Gersabeck and Aodhan Burke
(Dated: May 2024)

Abstract: This report presents a measurement of the bin-integrated production asymmetry between neutral D mesons in the Cabbibo-favoured decay mode $D^0 \to K^- \pi^+$. The analysis uses 600 million events from the Large Hadron Collider beauty experiment in 2016, 2017, and 2018. A reweighting process of various decay modes allowed the detection asymmetry for each year and magnet polarity to be measured. These results are averaged to find total pseudo-detection asymmetry, which is calculated to be,

$$A_{det}(D^0) = -0.50 \pm 0.12 \text{ \%},$$

where the uncertainty is statistical. Furthermore, the production asymmetry for each year and magnet polarity were measured. These results are averaged to find the overall pseudo-bin-integrated production asymmetry, which is calculated to be

$$A_{prod}(D^0) = -0.78 \pm 0.12 \pm 0.02 \text{ \%},$$

where the first uncertainty is statistical, and the second is the calculated systematic uncertainty. These results agree with the total pseudo-bin-integrated production asymmetry calculated by a prior analysis at a significance of less than two, which was found to be $A_{prod}(D^0) = -0.546 \pm 0.122 \pm 0.18$ %. The dataset was subjected to a binning scheme, and subsequently, the production asymmetry was evaluated in each phase-space bin to verify the presence of any kinematic dependence. However, comparisons between simulated data from PYTHIA and the measured production asymmetry in the phase-space bins show a disparity between the two datasets.

Contents

1 Introduction

1.1 Background and motivation

The Large Hadron Collider beauty (LHCb) experiment is dedicated to studying heavy flavour physics and is well suited to measure heavy-quark production asymmetries by using a forward-arm spectrometer covering the pseudorapidity range $2 < \eta < 5$ [1] [2]. The choice of the detector's geometry is because the b and c hadrons are primarily produced in the forward or backward cone during high energy collisions [1] [3], which are sensitive to colliding partons within the protons. This sensitivity provides a unique opportunity to perform asymmetry measurements by isolating the events of interest and reducing background [2].

Measurement of production asymmetry is vital to exploring the prevalence of CP Violation (CPV) in the quark sector, as the physical asymmetries must be removed from the observed asymmetry to see the effect of CPV. The Standard Model (SM) does not account for the significant amount of CPV anticipated to result in a matter-dominated universe. Therefore, comprehending CPV can enhance our understanding of the physics of SM and beyond the Standard Model.

This experiment expands upon prior research in Ref [4] by using more data to calculate the differences in production rates (production asymmetry) between the neutral D mesons in the proton-proton collision performed at the LHC. The analysis focuses on the decay mode of the D meson to a kaon and a pion. The key objective of the analysis is to reduce the statistical uncertainty of production asymmetry by using more data in the invariant mass distribution fit and calculation of detection asymmetry. Furthermore, to expand upon the kinematic dependence explored previously, a simulation is run using PYTHIA. Moreover, detector asymmetry substantially varies with phase space and could be used to vary detector asymmetry per bin to find a more conclusive dependency.

2 Theory

2.1 The Standard Model

The SM is built upon the framework of local relativistic quantum field theory [5], which has the global external symmetries of special relativity: spatial rotations, spacetime translations, and Lorentz transformations, as well as the internal symmetries from Quantum Mechanics (QM). The SM treats each particle as an excitation of a field with suitable transformation properties under the Lorentz group, which depends on the particle's spin [5]. The theory is based on a common principle, gauge invariance [5], which requires the Lagrangian density of each particle to be invariant under a local phase transformation. The SM requires the fundamental particles to be invariant under a local gauge transformation of $SU(3) \times SU(2)_L \times U(1)$ [3] symmetry group.

The elementary particles are split into bosons (integer spin) and fermions (spin 1/2). The fermions obey the Pauli Exclusion Principle and can be split into three generations [6]. Each generation contains one neutral lepton (ν_e, ν_μ, ν_τ), one charge lepton (e, μ, τ), one down-type quark (d, s, b), which has $-1/3$ elementary charge (e) and one up-type quark (u, c, t) which has charge $+2/3$e. Each generation has the same properties, except flavour, and the masses vary significantly [6]. The masses of the neutrinos are not precisely known. The Dirac equation for a charged massive fermion correctly predicts the existence of an antiparticle of the same mass and spin but opposite charge [7].

The gauge symmetries result in gauge bosons, which are the force carriers. Furthermore, Noether's theorem requires that each symmetry corresponds to an invariant property [7]. The SM's three interactions are the EM, weak, strong.

The electroweak (EW) interactions are generated by a $SU(2)_L \times U(1)$ symmetry, which results in a massless natural force carrier for the electromagnetic interaction, photon, and conserves properties such as electric charge. The EW interaction also results in $W^{\pm}$ and Z for the weak interaction, which are massive and have an invariant property, weak isospin. The Higgs boson is a scalar boson produced by the Higgs field. Particles in the SM acquire their mass by coupling with the Higgs. The particle was theoretically predicted by the SM to accommodate a spontaneous symmetry breaking in $U(1) \times SU(2)_L$ local gauge symmetry that justifies the mass of the weak force carriers [8] [6].

The strong interactions are described by an $SU(3)$ local gauge theory called quantum chromodynamics (QCD), which uses three colour charges (red, green, blue) [6]. Eight gauge bosons are derived from QCD, which are the massless, neutral, spin one gluons, which carry a colour and an anticolour charge [5]. The vacuum polarisation effect (VPE) alters the effective charge by quantum corrections resulting from virtual particles emerging from the vacuum [7]. Although QED exhibits similar effects, the impact of the VPE in QCD is more significant due to its stronger coupling. The effective strong coupling can defined as,

$$\alpha_s(Q^2) = \frac{g^2(Q^2)}{4\pi} = \frac{4\pi}{[11 - (2/3)n_f]\ln(Q^2/\Lambda^2)}, \tag{1}$$

where n_f is the effective number of quark flavours depending on the energy of the scattering process, Q^2 is the momentum transfer squared, and Λ is the fundamental constant of QCD. In contrast to vacuum polarisation effects from QED, $g(Q^2)$ decreases as Q^2 increases; the virtual gluons contribution outweighs the negative contributions from the virtual fermions ($-(2/3)n_f$). This phenomenon is unique to QCD and can be attributed to the distinctive gluon self-interaction that permits gluon loops. It is this feature that is responsible for the asymptotic freedom observed in Equation 1, where $\alpha_s(Q^2) \to 0$ as $Q^2 \to \infty$ [7]. The asymptotic freedom is a crucial aspect of the strong force since it leads to the weakening of forces between partons as they get closer to each other. This leads to the key concept of confinement, which predicts that no isolated coloured charge exists, including gluons [5]. Confinement occurs as it is energetically favourable for quarks separated from each other close to the confinement length, $1/\Lambda$, to create quark and antiquark pairs to form colourless hadrons [9] [10].

Despite the success of the Standard Model (SM) in explaining various physical phenomena, such as the existence of the Higgs boson and the precise prediction of the electron's magnetic moment, it is widely acknowledged that the SM is an incomplete theory. The SM only accounts for 5% of the universe's mass-energy content, as dark matter and energy are not incorporated into the model [11]. Furthermore, a theory of quantum gravity is not well understood as the forces of gravity at sub-particle levels are very weak, and the theory has to be compatible with special relativity, which treats gravity as changes in the fabric of spacetime.

2.2 Production Asymmetry

Fixed target experiments have observed large amounts of charmed baryon and meson asymmetries in the forward regime [12]. Production asymmetry, denoted by A_{prod}, arises due to the distinct hadronisation probabilities between D^0 and $\bar{D}^0$ [13]. The production asymmetry is defined using the cross sections,

$$A_{prod}(D^0) = \frac{\sigma(D^0) - \sigma(\bar{D}^0)}{\sigma(D^0) + \sigma(\bar{D}^0)}, \tag{2}$$

where the $\sigma(D^0)$ and $\sigma(\bar{D}^0)$ are the cross section of the D and $\bar{D}^0$ respectively. The calculation of cross-sections is challenging owing to the poor description of charm quarks by the lowest-order perturbation QCD
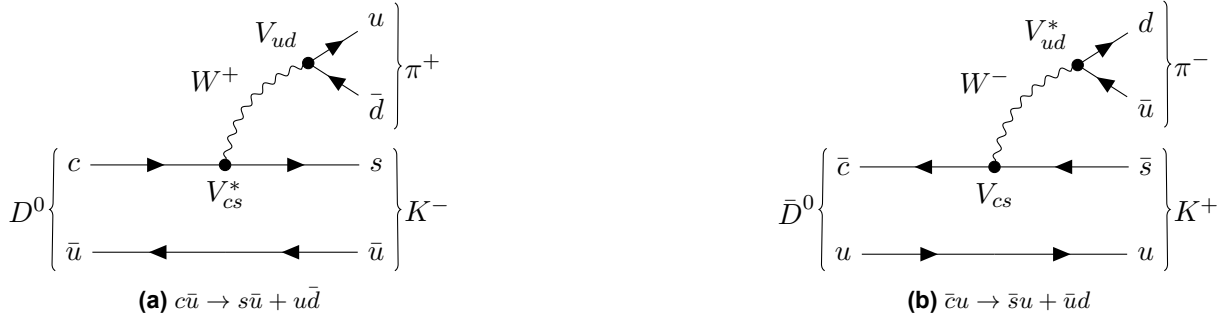
(a) $c\bar{u} \to s\bar{u} + u\bar{d}$ **(b)** $\bar{c}u \to \bar{s}u + \bar{u}d$

Fig. 1. Feynman diagrams showing the leading order decays of the neutral D meson decaying to a kaon and pion and the corresponding CKM matrix elements corresponding with each decay.

mechanism [14]; however, factorisation theorems of perturbative QCD demonstrate that heavy hadron cross-sections can be expressed in a factorised form, allowing the cross-section to be predicted [12]. As a result, in this analysis, the asymmetry in the signal yield (A_{raw}) is used as a probe to calculate the A_{prod} by performing an extended maximum-likelihood fit to the invariant mass of the neutral D mesons,

$$A_{raw}(D^0) = \frac{N(D^0) - N(\bar{D}^0)}{N(D^0) + N(\bar{D}^0)},\tag{3}$$

where the $N(D^0)$ and $N(\bar{D}^0)$ are the signal yield of the D^0 and $\bar{D}^0$ respectively. The raw asymmetry measured is a combination of physical asymmetries and other contributions,

$$A_{prod}(D^0) = A_{raw}(D^0) - A_{Det}(D^0) - A_{CP}(D^0),\tag{4}$$

where $A_{Det}(D^0)$ is the detector asymmetry and $A_{CP}(D^0)$ is the asymmetry introduced by CPV. Additionally, the kinematic distributions of charmed hadrons and their antiparticles can vary, introducing production asymmetries in local kinematic regions, which will be investigated in this analysis [15]. To minimise residual detection asymmetries, the final asymmetry is computed by taking the arithmetic average of the outcomes acquired for both bending magnet polarities, namely MagUp and MagDown [16].

Figure 1 shows the Feynman diagram of the D meson decaying to a kaon and pion, where the transition probability associated with the decay of D^0 is $|V_{ud}V_{cs}^\star|^2$ and for the $\bar{D}^0$ is $|V_{ud}^\star V_{cs}|^2$. In Wolfenstein's parameterisation of the Cabibbo-Kobayashi-Maskawa (CKM) matrix, the complex phase is solely associated with the matrix elements V_{ub} and V_{td} [17]. Therefore, the decay mode of D meson to a kaon and a pion will not contribute to the CPV as $V_{cs} = V_{cs}^\star$ and $V_{ud} = V_{ud}^\star$. Additionally, a neutral meson can oscillate into its antiparticle and vice versa. However, depending on flavour, the oscillation probabilities differ, indicating that the oscillation process leads to a preferred final state [18]. In the charm mesons, the oscillation parameter, $|q/p|$, is measured to be 0.995 ± 0.016, indicating CPV via mixing is negligible in this analysis' decay mode [19].

2.2.1 Leading Particle Effect

(a) $\bar{c} \to \bar{D}^0\bar{u}$ **(b)** $c \to D^0 u$

Fig. 2. The Feynman diagrams show the charm and anticharm quarks' hadronisation via the fragmentation mechanism, where the mechanism is shown to be independent of the production process [10] [20].

The leading particle effect is used to explain the asymmetries in hadronisation probabilities between D^0 and $\bar{D}^0$, which describe the hadrons that contain quarks that are in common with the beam hadron are produced in more significant numbers [13]. This predicts that the $\bar{D}^0$ meson will have a higher cross-section as the u quark in the meson matches the proton's quark content (uud). Conversely, the D^0 meson must form from a $\bar{u}$ quark generated in the pp collision, resulting in a lower production cross-section.

Factorised theorems of perturbative QCD at leading order in a $1/pT$ expansion allow the cross sections to be factorised into two parts. The first part is short-distance partonic cross sections that describes the production of heavy quarks and can be calculated perturbatively. The second part is a fragmentation function that cannot be calculated perturbatively as it involves long-distance physics. This information is from Ref. [21]. The differential cross-section of the D^0 meson is,

$$d\sigma[pp \rightarrow D + X] = \sum_{ij} f_{i/p} \, f_{j/p} \otimes d\hat{\sigma}[ij \rightarrow c\bar{c} + X] \otimes D_{c \rightarrow D}, \tag{5}$$

where the $f_{i/p}$ and $f_{j/p}$ are the parton distribution functions of quarks i and j, $d\hat{\sigma}[ij \rightarrow c\bar{c} + X]$ is the partonic cross sections, and $D_{c \rightarrow D}$ is the fragmentation function describing hadronisation of charm quark into D meson [12] [13]. The parton distribution functions provide knowledge on the probability of a specific parton from the colliding protons interacting during the inelastic scattering [22]. The probability of obtaining a parton varies on the fraction of the total proton momentum, x, it carries. At high x, the partons involved in the collision are likely to be the valence quarks, u or d. Meanwhile, at low x, the contribution from gluons and sea quarks increases greatly [23]. The corresponding equation for $\bar{D}$ is obtained by replacing $D_{c \rightarrow D}$ with $D_{\bar{c} \rightarrow \bar{D}}$ [13].

(a) Gluons combine to give two charm quarks.   **(b)** Quarks combine to give two charm quarks.

Fig. 3. Leading order diagrams for $c\bar{c}$ production with (a) the gg contribution and (b) the $q\bar{q}$ annihilation. Two more LO diagrams have gg initial states, showing that the c and $\bar{c}$ are produced symmetrically in a proton-proton collision [24].

The fragmentation mechanism is one way to describe the charm quark's hadronisation, as shown in Figure 2 [25]. The fragmentation process predicts strict independence of the heavy quark hadronisation from the production process [10]. A quark-antiquark is produced and generated in each quark from the parton shower until the available momentum is used up [25]. The perturbation theory is accurate in the transverse momentum limit of $p_T \rightarrow \infty$. For finite momentum, the fragmentation mechanism expects corrections that are suppressed by a factor of Λ_{QCD}/p_T [21], and therefore can expect non-vanishing correction to production asymmetry at low p_T [12].

However, the fragmentation mechanism does not predict production asymmetry at LO as the $c\bar{c}$ production is charge symmetric, as seen in Figure 3, and results in $D_{c \rightarrow D} = D_{\bar{c} \rightarrow \bar{D}}$. Some asymmetries are seen in next-to-leading-order but are small relative to the observed production asymmetry [12]. Therefore, to explain the leading particle effect in charm hadrons, additional hadronisation models are required [13] as well as phenomenologically mechanisms like Lund string fragmentation (LSF) or the meson cloud.

2.2.2 Heavy Quark Recombination

The heavy quark mechanism (HQR) is a QCD-based model that incorporates corrections of the order $\mathcal{O}(\Lambda_{QCD} \, m_c/p_T^2)$ to the production cross section [12]. Braaten first introduced the HQR mechanism in
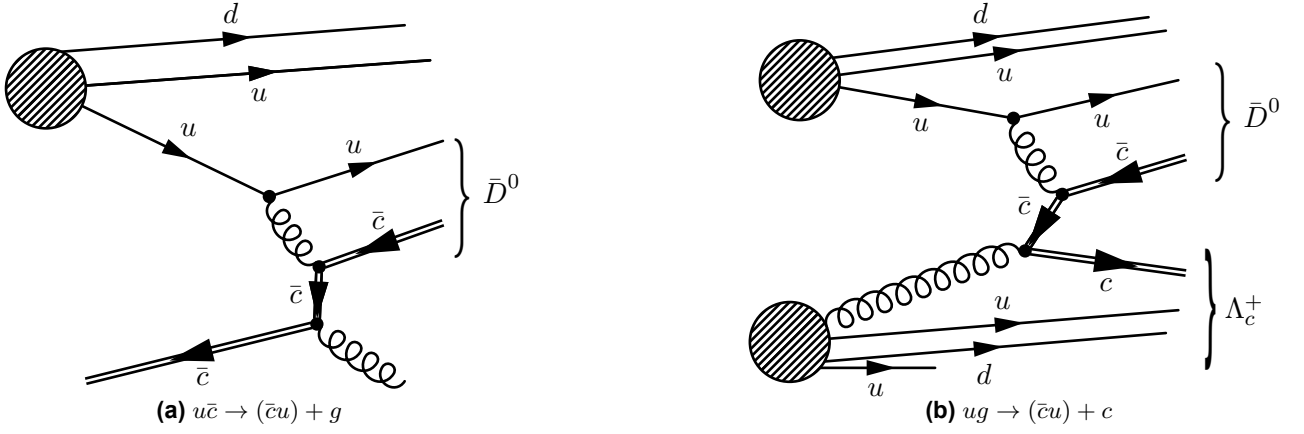
Fig. 4. The portrayed Feynman diagrams show the hadronisation of charm mesons via the HQR mechanism. In this process, the D meson is produced by the interaction of a spectator quark from the proton with a (a) charm quark or (b) gluon. Moreover, each process involves five diagrams, as described in Ref. [12]. Fig 4b also illustrates the production asymmetry observed in the Λ_c baryon [10]. Similar Feynman diagrams can be drawn for the D^0 meson.

Ref [21] to explain the observed asymmetries in the B meson; the mechanism has also been used to accurately predict charm asymmetries observed in the hadroproduction experiment E791 in Fermilab [12] [13]. The mechanism, as seen in Figure 4, shows the $\bar{c}$ produced in the pp collision hadronises with a light quark, u emerging from the collision with small momentum in the charm quarks frame [26]. A similar process is present for the hadronisation of c quark, where spectator quark, $\bar{u}$, from the proton hadronises with the c quark resulting in D^0 meson. Asymmetries occur in this mechanism, as the parton distribution functions of a u in a proton are much greater than those of the $\bar{u}$, which leads to an imbalance favoured towards $\bar{D}^0$ mesons. Figure 4b also provides a natural explanation for the observed asymmetries in the Λ_c baryon, as the c quark is likely to combine with a u and d to produce a Λ_c^+. In contrast, the $\bar{c}$ quark is less likely to form an anti-baryon [10].

The HQR mechanism contribution to the cross-section of $\bar{D}$ can be produced by factorisation theorems,

$$d\sigma[pp \to D] = f_{\bar{c}/p} \, f_{q/p} \otimes \sum_n d\hat{\sigma}[q\bar{c} \to (\bar{c}q)^n + g]\rho[(\bar{c}q)^n \to \bar{D}], \tag{6}$$

where the $f_{\bar{c}/p}$ and $f_{q/p}$ are the parton distribution functions of the $\bar{c}$ and u quark [26] [12]. The notation $(\bar{c}q)^n$ indicates a state the light quark has momentum $\mathcal{O}(\Lambda_{QCD})$ relative to the charm quark and that the charm and light quark are in a state with colour and quantum specified by n [21]. The cross-section is factored into the perturbatively calculatable $d\hat{\sigma}[q\bar{c} \to (\bar{c}q)^n + g]$ and the nonpertubative factor $\rho[(\bar{c}q)^n \to \bar{D}]$ that describes the probability for the quark pair to hadronise into the final state [12]. The HQR mechanism contains two more contributions to the σ [12] [13]:

$$d\sigma[pp \to \bar{D}] = f_{q/p} \, f_{g/p} \otimes \sum_n d\hat{\sigma}[gq \to (\bar{c}g)^n + c]\rho[(\bar{c}q)^n \to \bar{D}] \tag{7a}$$

$$d\sigma[pp \to \bar{D}] = f_{\bar{q}/p} \, f_{g/\,p} \otimes \sum_{n,\bar{q}} d\hat{\sigma}[\bar{q}g \to (c\bar{q})^n + \bar{c}]\rho[(c\bar{q})^n \to D, D*] \otimes D_{\bar{c}\to\bar{D}}. \tag{7b}$$

Equation 7a is the process, illustrated in Figure 4b, where the gluon and u from the proton are the initial states that hadronise into $\bar{D}$ and charm quark. The neutral D meson can also be produced by the charm quark, in Equation 7a, hadronising by the fragmentation mechanism. This process is shown in Equation 7b, where an antiquark and gluon form a D or D^* meson, and the $\bar{c}$ fragments to produce a $\bar{D}^0$. It is worth noting that the asymmetry resulting from the gluon quark interaction, as expressed in Equation 7a, tends to be diluted by the asymmetries generated during the fragmentation process as articulated in Equation 7b. The contributions to

$\sigma(D^0)$ can be obtained by taking the charge conjugation of the three equations above [12].

HQR mechanism predicts asymmetries in the hard scattering process, which allows kinematic dependence of asymmetry to be calculated by perturbative QCD [13]. The corrections to the fragmentation mechanism (Λ_{QCD}/p_T) and HQR mechanism $\mathcal{O}(\Lambda_{QCD} \ m_c/p_T^2)$ at low p_T implies variance of production asymmetry between high and low transverse momentum. Kinematic dependence of production asymmetry is observed in $D^{\pm}$ meson by the analysis conducted by Lai in Ref. [12]. This result is a primary motivation to explore and search for the same dependence in the natural D meson.

2.2.3 Lunds String Fragmentation

$$\bar{c}(\bar{r}) \ \underline{\quad \overset{\bar{D}^0}{\quad} \quad} \ u(r) \quad \bar{u}(\bar{r}) \ \underline{\quad \overset{\bar{p}}{\quad} \quad \overset{\bar{u}(\bar{b})}{\bar{d}(\bar{g})} \quad \overset{u(b)}{d(g)} \quad} \ \underline{\quad \overset{\Lambda_c{}^+}{\quad} \quad} \ c(r)$$

Fig. 5. A simplified diagram of a string breaking to form hadrons, adapted from Ref. [27]. The hadron formed from fragmentation is a colour connected to the original string.

The Lund string model is a string model that incorporates QCD confinement by spanning strings that represent the confining colour field between the partons [28] [29]. These strings have a constant string tension, $k \approx 1 \text{GeV/fm}$, and contain a colour triplet endpoint and an antitriplet colour endpoint, as seen in Fig 5. The double colour charge of gluons corresponds to gluons being attached to two strings (from the quarks), while a quark is only attached to one string [28]. As the partons are separated, the tension in the string increases until it is energetically allowed to create one or two quark pairs [25]. Each string's fragmentation continues until only on-shell hadrons remain [25]. In the LSF, the formation of hadrons is not independent of the protons, and the charm quarks produced are colour-connected to the proton beam [30]. For example, in a $u\bar{u} \to c\bar{c}$ process, the colour of the charm quark is inherited from the colour of the u from the proton [29].

Depending on the string's mass, the LSM has three modes of hadronisation: normal string fragmentation, cluster decay, and cluster collapse [29]. Normal string fragmentation occurs when the string has a large invariant mass, allowing the assumption of a continuum of phase-space states during the string fragmentation process [28]. This assumption breaks down at low mass, where the phase space inhibits the fragmentation, which can only form a few states [30]. These low-mass states are known as clusters and decay into a heavy and light hadron [28]. The third model is an extreme case where the mass of the string is tiny, allowing only a single hadron to be formed that inherits the flavour content of the string's endpoint. This third model allows asymmetries in favour of hadrons that can inherit flavour content from the beam and is dependent on the system's kinematics [31].

The beam drag effect caused by diquark effects leads to an asymmetry favouring D mesons, in contrast to the cluster collapse favouring $\bar{D}$ mesons [29]. Diquarks (qq) were initially introduced by phenomenological studies of strong interactions, such as the description of a proton as a quark-diquark state [32] [33]. However, the SU(3) theory predicts that a diquark is not a colour singlet state but an antitriplet state. As a result, they
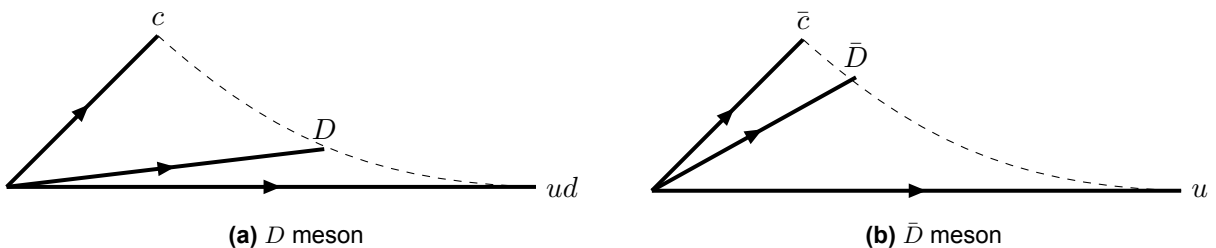

(a) D meson

(b) $\bar{D}$ meson

Fig. 6. A diagram illustrating the beam drag effect caused by the diquarks, leading to asymmetries favouring the non-leading meson in certain kinematic regimes. The meson is formed by string fragmentation between the colour-connected particles.

cannot be observed directly, and in this regard, they behave similarly to antiquarks [33] [28]. In allowed string configurations, the c quark has colour connections to diquarks and the $\bar{c}$ to quarks [29] [31]. The diquark's average energy and momentum are larger than the u quark, which allows the D meson to pick up more of the beam's momentum relative to the $\bar{D}$ meson, as seen in Figure 6. This results in an asymmetry as a function of momentum and rapidity [30] [31]. This effect is the rationale behind the D meson being favoured in specific kinematic regimes [29] [31]. Furthermore, the asymmetry strongly depends on the choice of beam remnant distribution function [30].

The string model provides a qualitative description of hadronisation; however, its precise implementation relies on parameters to be tuned to fit the dataset [34], such as the beam remnant distribution function. Additionally, more research is required to comprehensively comprehend the low-mass hadronisation, particularly concerning the diquark endpoints [34].

3 The LHCb Experiment

To observe D mesons, which have a neutral lifetime of $(410.3 \pm 1.0) \times 10^{-15}$s [19], the LHCb experiment relies on identifying their decay products. This is accomplished by using silicon detectors and calorimeters in tandem, which allows for the precise reconstruction of the decay products with exceptional vertex, momentum, and invariant mass resolutions [1]. The spectrometer consists of tracking and particle identification (PID) systems and the trigger system, which selectively saves only the events of interest to conserve processing power and storage [35]. One of the less desirable characteristics of the LHC environment is the inherent increase in background levels encountered during hadronic collisions. This phenomenon leads to experimental compromises, including difficulties in reconstructing final states that involve missing or neutral particles [36]. The following text will outline the path of a charged particle through the detector, as the detection and tracking of neutral particles involve distinct processes [37].

3.1 Tracking System

The trajectories of charged particles are reconstructed using the tracking system, which consists of the Vertex Locator (VELO), Tracking Turicensis (TT) before a dipole magnet, and the Inner and Outer Tracker (IT and OT) after the dipole magnet. The tracking system measures the momentum and charge of the charged particle.

The VELO provides precise track coordinates (r and ϕ) using a series of silicon modules close to the pp collision point, with a resolution of 10μm [3]. These sensors are used to identify secondary vertices of c and b hadron decays, which is essential in identifying the meson [1]. The silicon modules are mounted in a vessel that maintains a vacuum around the sensors to minimise the material travelled by a charged particle before it crosses the sensors.

Upon traversing the VELO, the charged particle proceeds to the Ring-Imaging Cherenkov (RICH) detector, described in the subsequent subsection, and the TT tracker. The TT silicon strips tracker estimates the particle's momentum, which is crucial for the trigger decision [38]. As the charged particle passes through the silicon detector, an electron-hole pair is created, drifting to a nearby electrode; this signal is used to track the particle's trajectory.

Following the TT detector, the charged particles are bent in the magnetic field of the main dipole magnet, with a bending strength of 4Tm [36]. The curvature of a charged particle's path in a bending magnet is analysed using the Lorentz equation to determine the particle's momentum. The spectrometer's magnet field significantly impacts the beams' trajectory. Three dipole magnets are employed to counteract this effect and ensure a closed orbit for the beams [36].

The last stage of the tracking system consists of a triad of T stations, each containing an IT and OT. The region near the beamline is surrounded by the IT, a silicon strip detector [38]. The IT is surrounded by gas-filled straw tubes, referred to as the OT [35]. The straw tubes are filled with 70% Argon and 30% CO_2 [1], which can be ionised by particles passing through to detect a signal.

The neutral D meson decay products are reconstructed as long tracks as the meson's decay time is sufficiently small [36]. Long tracks are reconstructed by combining hits in the VELO, TT-stations and T-stations, giving the best momentum and position estimate [39]. The tracking system measures momentum with an uncertainty that varies from 0.5% at 5 GeV/c to 1% at 200 GeV/c [39].

3.2 Particle Identification System

The PID determines the particle's composition using a combination of RICH detectors, a calorimeter system, and muon chambers. Using the information from the PID system, likelihood values are calculated for different particle hypotheses [3], which can be used for selection criteria or in the trigger.

The Cherenkov effect is the emission of photons when charged particles pass through a medium at a velocity v_p greater than the phase velocity of light in the medium [35]. Cherenkov radiation is emitted in a cone with a polar angle (θ_c) and can be related to the velocity and mass of the particle m,

$$\cos(\theta_c) = \frac{c}{v_p n} = \frac{1}{n}\sqrt{1 + \left(\frac{mc}{p}\right)^2} \tag{8}$$

where p is the measured momentum, and n is the material's refractive index [4]. At large θ_c, the momentum spectrum of a given particle is low, while at small θ_c, the momentum spectrum is harder [1]. The PID system consists of two RICH detectors at different locations to cover a momentum range of 1-100 GeV/c [1] [35], which allows the system to detect a range of particles.

The calorimeters provide identification of electrons, photons and hadrons as well as their energies and position [1]. Furthermore, the data provided is used in trigger decisions as discussed in Section 3.3. The calorimeters are placed downstream of the RICH2 detector and between the first and second muon stations. To assist in particle identification of the electron, which is vital for trigger decisions, the electromagnetic calorimeter (ECAL) has two detectors placed in front of them, namely the scintillator pad (SPD) and pre-shower (PS) detectors [35]. The SPD detector is made of scintillator tiles that assist in rejecting background candidates for electrons, such as $\pi \to \gamma\gamma$ [35] [1]. This is done by distinguishing electrons from photons, as only the prior can deposit energy in the SPD [3]. The PS detector is a lead converter that allows electrons to shower. This is used along with the ECAL to remove charged pions as electron candidates [35]. The ECAL measures the energy of photons and electrons, while the hadron calorimeter (HCAL) measures the energy of hadrons [3].

The muon system consists of five stations. The M1 is placed upstream of the calorimeters and is used to improve the muon's p_T measurements required for the trigger. The M2-M5 stations are placed downstream of the calorimeters and interleaved with 80 cm thick iron absorbers to ensure only the minimally interacting muons are detected [1] [3]. M1-M3 stations have high spatial resolution along the magnet's bending plane. They are used to define the track direction and calculate p_T of the muon. Meanwhile, the primary purpose of the M4-M5 stations is the identification of muons [1].

3.3 Trigger

The LHCb trigger consists of three levels: a hardware trigger (L0) and two software triggers (HLT1 andLT2). The triggers are required to reduce the rate of events to save processing power and storage. The L0 trigger is implemented 4μm after the interaction, using custom-made electronics that reduce the beam crossing rate from 40MHz to 1MHz [1]. The L0 trigger reconstructs and selects particles with high transverse momentum in the muon chambers or high transverse energy in the calorimeter system to remove background events [40]. HLT1 and HLT2 are C++ applications running at the Event Filter Farm (EFF) to reduce the events from L0 trigger [1]. HLT1 performs a partial event reconstruction using the VELO and T stations to reduce the required processing power [1] [41]. Meanwhile, HLT2 reduces the frequency further by fully reconstructing the events [40].

4 Previous Analysis

The prior analysis measured the production asymmetry between the neutral D mesons using the decay channels of the D^0 decaying to a kaon and pion. Moreover, a kinematic dependence of the asymmetry was explored. The previous analyses are found in Ref [4], and a summary of the methodologies and critical findings employed in the analysis are explained in this section.

4.1 Modelling the Invariant Mass Distribution

The previous analysis initially used an unbinned extended likelihood fit to model the invariant mass distribution (IMD) of the D meson. However, this was altered to a binned fit due to its computational advantages, which allowed the dataset to be increased. The analysis is centred around two models which have exhibited satisfactory pull distributions. The first model consists of a Johnson distribution and two Bifurcated Gaussian functions. In contrast, the second model comprises a Gaussian distribution, a Johnson distribution, and a Bifurcated Gaussian distribution. Although both models have yielded similar pulls, the peaks do not align in the second model, yielding the prior model as the more optimal choice for production asymmetry analysis. However, both models exhibited an oscillatory pull distribution, indicating that the fit could have been further improved.

4.2 Binning Scheme

Three separate binning schemes were used for the previous analysis to explore the kinematic dependence. The first binning scheme was two-dimensional with 100 bins in the p_T and η phase space. The bin boundaries for each year were calculated using data from both mesons and polarities and were altered to ensure an approximate even number of candidates in each bin. The second binning scheme creates ten phase-space bins for p_T, while the third creates ten bins in the phase space of η.

An extended maximum-likelihood fit is performed for each bin to measure the production asymmetry across the phase space. However, splitting the data into many bins led to significant Poisson errors in the background, and the model was found to be discontinuous at peaks in particular bins. This analysis will attempt to address these issues by increasing the original dataset before the binning scheme is applied.

4.3 Results

The production asymmetries measured from the previous analysis are shown in Table 1. These results indicate that more $\bar{D}^0$ mesons were produced than the D^0 meson, as expected from the leading particle effect. A search for kinematic dependence on production asymmetry using a linear fit did not give a conclusive result, as the reduced chi-squared was generally too low due to the large errors. This analysis will attempt to address these issues by attempting to reduce the uncertainty of detector asymmetry.

	Production Asymmetry [%]
2016	$-0.866 \pm 0.204 \pm 0.013$
2017	$-0.376 \pm 0.213 \pm 0.020$
2018	$-0.397 \pm 0.219 \pm 0.013$
Total	$-0.546 \pm 0.122 \pm 0.018$

Table 1. A table showing the production asymmetry from the prior analysis for each year that was obtained by modelling the invariant mass distribution using Model 1. The arithmetic average was performed on the results for each year to find the total asymmetry.

5 Modelling the Invariant Mass Distribution

An extended maximum likelihood fit is used to fit the data and the parameter for a given model and is generated using `RooFit`, a package for statistical modelling distributed with ROOT [42]. To assess the quality of the model, a pull for each data, δ_i, can be calculated as,

$$\delta_i = \frac{y_i^{data}(x_i) - y_i^{expected}(x_i)}{\sigma_i^{expected}}, \tag{9}$$

with $y_i^{expected}$ and $\sigma_i^{expected}$ being the value and uncertainty of the probability distribution function at the given x_i, and the $y_i^{data}(x_i)$ is the value of the ith bin [4]. A pull distribution plot is created that represents the distribution of entries with a specific δ_i. A Gaussian fit is plotted on the pull distribution using the `curve_fit` function from SciPy [43]. The best model will have the pull distribution resembling a closet to a normal distribution, resulting in the Gaussian's μ and σ equal to one and zero, respectively.
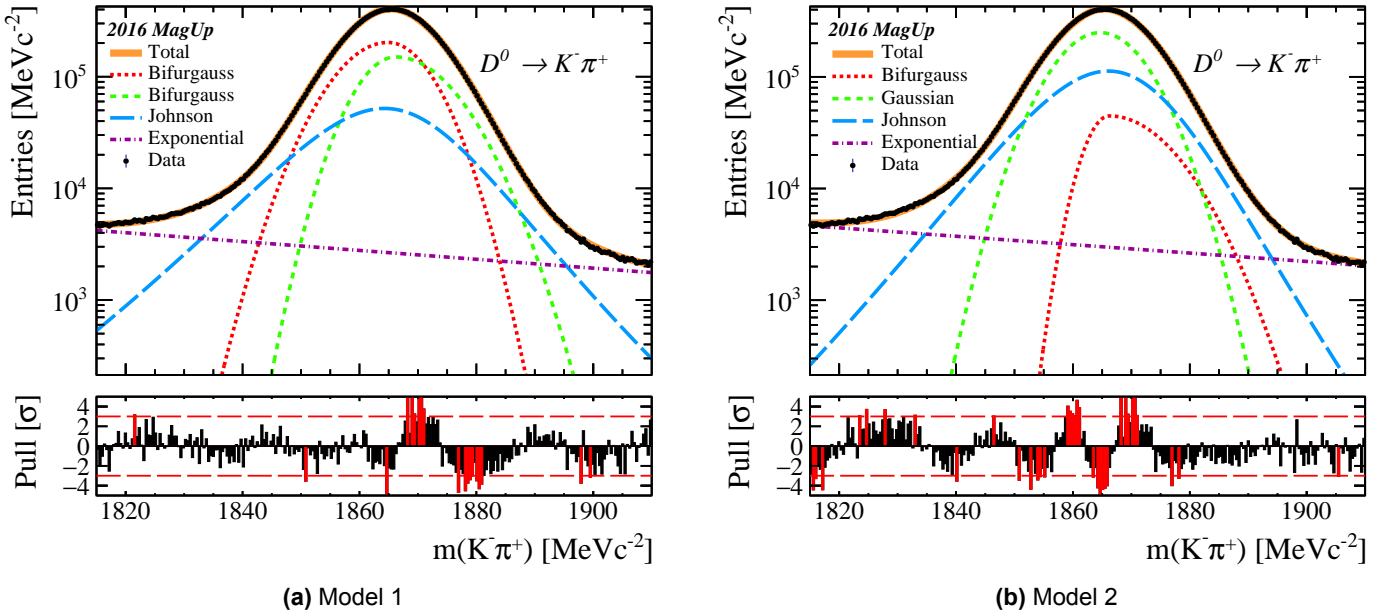

Fig. 7. Invariant mass distributions of D^0 meson, using the 2016 MagUp data and fitted using the models from the previous analysis on a quadrupled dataset.

The model from the prior analysis yielded a fit that demonstrated reasonable performance, exhibiting good pulls, as described in Section 4.1. However, the primary objective of this analysis was to increase the IMD dataset. After quintupling the original dataset, it was observed that the models exhibited poor performance, as evidenced by a significant number of bad pulls, and required a new model. Consequently, this analysis only quadrupled the dataset, which using the same model allowed satisfactory pulls to be observed, as seen

in Figure 7a. Model 2, illustrated in Figure 7b, is the model used to calculate the systematic uncertainty as the means of the three peaks representing the signal do not align. However, the increase in data resulted in a worse model, as seen in the mean and sigma of the pull distribution relative to the previous analysis. This can be observed in Table 9. Moreover, the oscillatory behaviour of the pulls suggests a subpar fit.

Attempts were made to create a new model for a larger dataset and fix the previous model's issues. Many models, such as a Gaussian, Gaussian, and Crystal Ball function, were tried, which delivered poor pull distributions. However, a Gaussian added to Model 1 to represent the signal led to respectable results, shown in Figure 8a. However, the model did not fit the data from 2018, and a kinematic relationship could not be found using the model. This is because when the model is used to fit one of the phase-space bins, the fit fails or poor pulls occur, as shown in Figure 8b. Therefore, the rest of the analysis uses Model 1 previously discussed, with Model 2 used to measure systematic uncertainty.
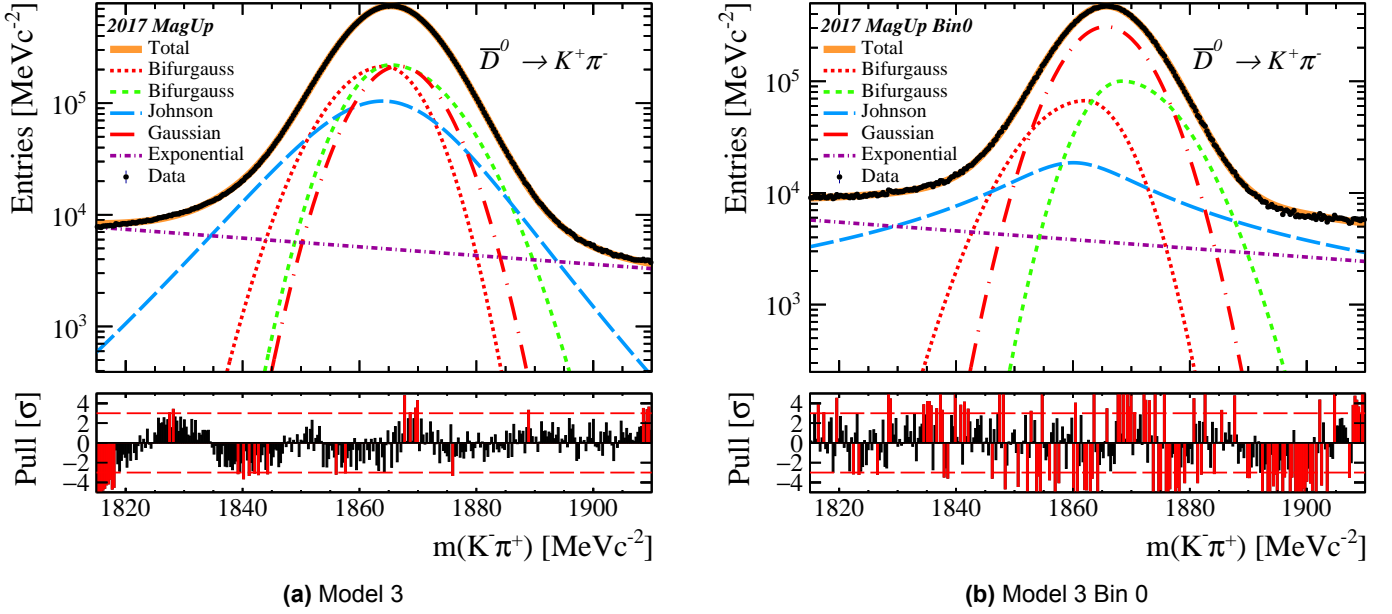

(a) Model 3

(b) Model 3 Bin 0

Fig. 8. (a) Invariant mass distributions of D^0 meson, using the 2016 MagDown data and fitted using the model representing the signal with an extra Gaussian function. (b) Model 3 was applied to a phase-space bin in the 2017 MagUp dataset.

6 Detection Asymmetry

A contribution of detection asymmetry is from the different trajectories of positively and negatively charged particles, thus having different sensitivities to the inhomogeneities of the detector [44]. It is partially cancelled when taking the arithmetic average between both polarities. Another detection asymmetry contribution is the result of charge asymmetric nuclear cross sections between the detector material and the decay products of the neutral D meson results in detection asymmetry [45]. The detector has an approximately equal distribution of two types of baryonic matter: protons (p) with valence quarks of uud and neutrons (n) with valence quarks of udd. The strong interaction at LHC energies dominates the annihilation of a quark-antiquark. The decay product, $\pi^{\pm}$, interacts symmetrically via annihilation as the quark compositions ($\bar{u}d$ and $u\bar{u}$) contain a valance antiquark that matches the valance quarks of the detector. In contrast, the quark composition of K^+ and K^- differs as the K^+ contains a u quark and the K^- contains a $\bar{u}$ quark. The $\bar{u}$ quark is more likely to interact with the detector material, while the u quark from the K^- requires a $\bar{u}$ sea quark to annihilate via the strong interaction. The interaction of the strange quark and antiquark can be assumed negligible as the interactions for both require a strange sea quark. Experimentally, access to the combined detection asymmetry of $K^-\pi^+$ was more feasible than measuring the detection asymmetry of a kaon. The combined asymmetry is the

difference between the detection efficiencies of $K^+\pi^-$ and $K^-\pi^+$

$$A_{det}(K^-\pi^+) = \frac{\varepsilon_{det}(K^-\pi^+) - \varepsilon_{det}(K^+\pi^-)}{\varepsilon_{det}(K^-\pi^+) + \varepsilon_{det}(K^+\pi^-)}, \tag{10}$$

where the ε_{det} is the efficiency of the detector measuring the track. The K^- has a higher nuclear cross-section and will interact inelastically with the detector material before enough hits are present for the track to be reconstructed [44]. Consequently, $A_{det}(K^-\pi^+)$ is expected to be negative as K^+ are tracked better.

To a good approximation, the detection asymmetry of a decay mode can be decomposed into the detection asymmetry of the separate decay products [45]. Therefore the detection asymmetry of $A_{det}(K^-\pi^+)$ can be calculated by using the decay mode $D^+ \to K^-\pi^+\pi^+$ and decomposing $A_{det}(K^-\pi^+\pi^+)$,

$$A_{det}(K^-\pi^+) = A_{raw}(D^+ \to K^-\pi^+\pi^+) - A_{det}(\pi^+) - A_{prod}(D^+) + A_{trigger}, \tag{11}$$

where $A_{trigger}$ is asymmetry related to the trigger [45]. A second decay channel $D^+ \to K_s^0\pi^+$ is required to eliminate unnecessary terms, such as the detection asymmetry of π^+. Consequently, the detection asymmetry of $K^-\pi^+$ can be calculated using known quantities,

$$A_{det}(K^-\pi^+) = A_{raw}(D^+ \to K^-\pi^+\pi^+) - A_{raw}(D^+ \to K_s^0\pi^+) + A_{det}(K_s^0), \tag{12}$$

where the raw asymmetries can be measured accurately as the D^+ is produced abudently in the LHCb and the $A_{det}(K_s^0)$ has a known value of 0.054 ± 0.014 [45].

6.1 Kinematic Reweighting

The phase-space-dependent detection and production asymmetries affect the measured asymmetry in D^+ decays. Therefore, to calculate the raw asymmetries in Equation 12, the kinematic variables of the two control modes must be reweighted using (p, η, ϕ) and (p_T, η, ϕ) where ϕ is the azimuthal angle.

The reweighting process was obtained using the `hep.ml.reweight` machine learning `PYTHON` library, which requires a lot of computing power. The results obtained for the reweighting of the first control mode, $D^\pm \to K^\mp\pi^\pm\pi^\pm$, are presented in Figure 9, where the blue distributions are the kinematics of the control mode before reweighting, green is the kinematics after reweighting, and red lines are the desired kinematics that belong to the decay mode $D^0 \to K^\mp\pi^\pm$. The resulting green distributions are achieved by assigning weights to the blue distributions to align them with the red line. The reweighting procedure needs to be carried out for both the kinematic distribution of the kaon, utilising the kinematic variables (p, η, ϕ) as depicted at the top of Figure 9, as well as for the pion, making use of (p_T, η, ϕ) as shown in the bottom panel of Figure 9. A similar procedure was used to reweight the kinematics of the $D^\pm \to K_s^0\pi^\pm$ to the reweighted kinematics of the first control mode. The reweighting results of the second control mode are shown in Appendix C Figure 13. Ratios of the control mode relative to the desired kinematic regimes are shown in Figure 9. The green points (weighted kinematics over desired kinematics) should be constant at 1 for an exact reweighting process. However, this analysis shows an oscillatory pattern in the ratios for ϕ, suggesting the reweighting procedure can be improved. Furthermore, memory issues required the reweighting procedure to use only one million events to find the global asymmetry.

Once the reweighting procedure is completed, the raw asymmetry can be obtained by fitting the weighted invariant mass distribution for both control modes. The first control mode utilises a Gaussian and Johnson function for signal modelling, whereas the second control mode uses a Crystal Ball and Bifurcated Gaussian function. An exponential is employed to model the combinatorial background of both decay modes. The fit parameters are calculated using an initial likelihood fit, followed by a chi-squared fitting procedure that utilises
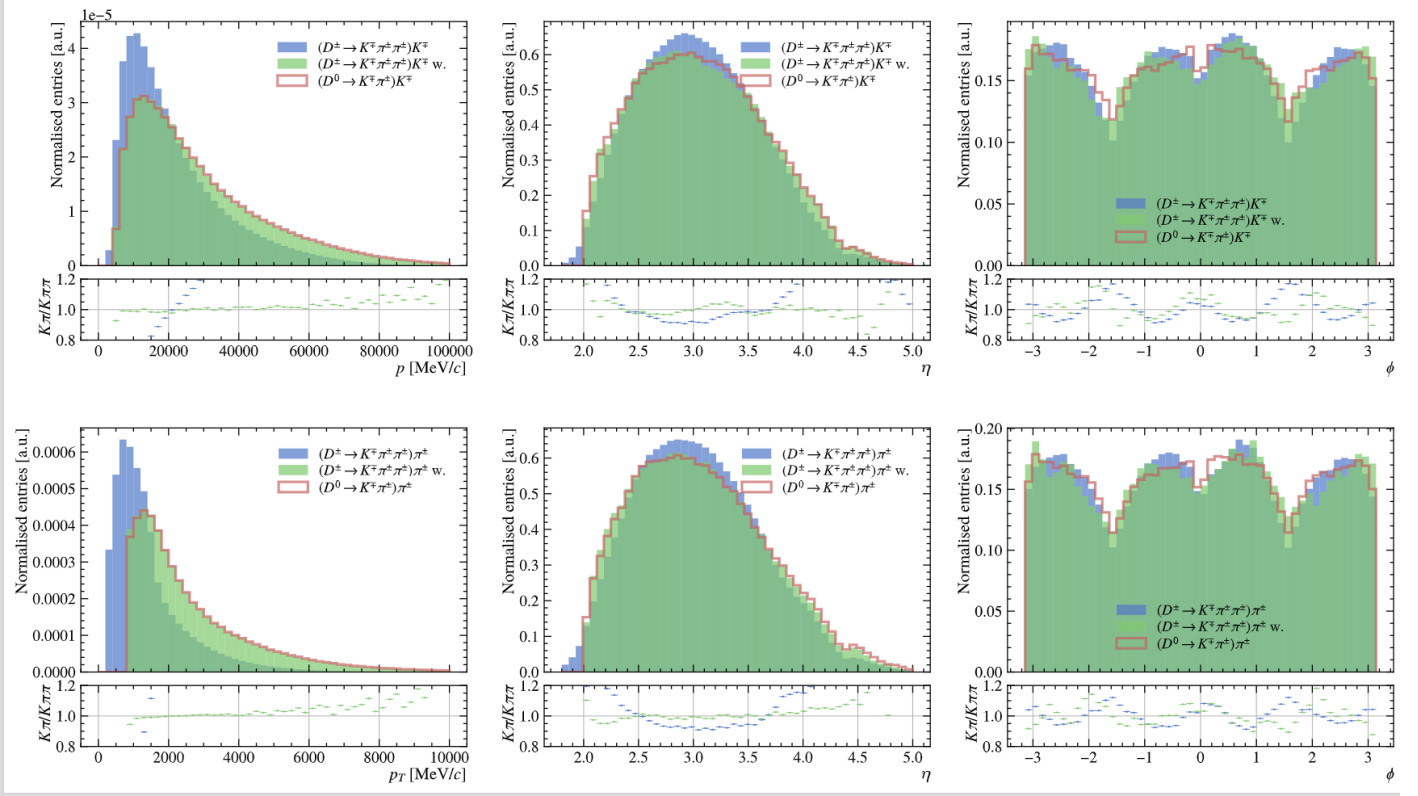
Fig. 9. The reweighted kinematic distributions of (p, η, ϕ) and (p_T, η, ϕ) for the $D^\pm \to K^\mp \pi^\pm \pi^\pm$ control mode using the 2017 MagDown dataset. The ratios of control mode over the desired kinematic regime are also shown in the graph.

the initial guess from the previous fit. The results of the fitting process for the two control modes are shown in Appendix C.1, where the pull distribution of the models suggests a good model has been implemented.

Year	Polarity	$A_{det}(K^-\pi^+)$ [%]	Polarity Integrated A_{det} [%]
2016	MagUp	-1.95 ± 0.29	-0.78 ± 0.19
	MagDown	0.39 ± 0.25	
2017	MagUp	-2.75 ± 0.31	-1.34 ± 0.22
	MagDown	0.07 ± 0.32	
2018	MagUp	-0.02 ± 0.31	0.63 ± 0.22
	MagDown	1.27 ± 0.32	

Table 2. A table containing the detection asymmetry for a year and polarity combination. A polarity-integrated detection asymmetry is also presented.

The raw asymmetries allow the detection asymmetries to be calculated using Equation 12, and the error through quadrature. The statistical uncertainty of the raw asymmetries is generated by `ROOT`, while $A_{det}(K_s^0)$'s uncertainty is the previously stated value. This results in detection asymmetries shown in Table 2. The polarity integrated detection asymmetry is calculated by taking the arithmetic average of each polarity measurement. A discrepancy is observed for the 2018 polarity integrated detection asymmetry value, as a positive value implies K^- are tracked better by the detector. This disagrees with the expectations from Equation 10. A total pseudo-detection asymmetry is calculated with a -0.50 ± 0.12 value.

6.2 Variation of Detection Asymmetry with Phase Space

A primary objective of this analysis was to determine the relationship between detection asymmetry and phase space by calculating the detection asymmetry separately in each phase space bin. The binned data from the binning scheme discussed in Section 4.2 was subjected to kinematic reweighting and modelling, as elaborated in Section 6.1. The detection asymmetry values for each bin are presented in Appendix C.2. The outcome of

this relationship for 2016 data is presented in Figure 10. Two key observations can be seen from the graphs. The data points agree with the hypothesis that K^+ are better tracked as the data points are mainly negative. However, the data cannot confidently predict a kinematic dependence as significant uncertainties dominate the edge bins. The large uncertainties can be attributed to the low number of counts per bin in the invariant mass distribution of $K_s^0\pi^\pm$ decay mode, resulting in relatively significant Poisson statistics uncertainties. As a result, a bad fit of the IMD's background can still lead to a good pull distribution. Attempts were made to reduce the uncertainty by using the global fit parameters. However, this approach proved to be unsuccessful as the global detection asymmetry is not a bin-integrated result but rather a sample containing a similar number of events compared to the binned datasets. Another source of uncertainty is caused by the reweighting of $K_s^0\pi^\pm$ to the already reweighted kinematics of $K^\mp\pi^\pm\pi^\pm$. Hence, any impreciseness in the initial reweighting is propagated to the second reweighting procedure, further increasing uncertainty.
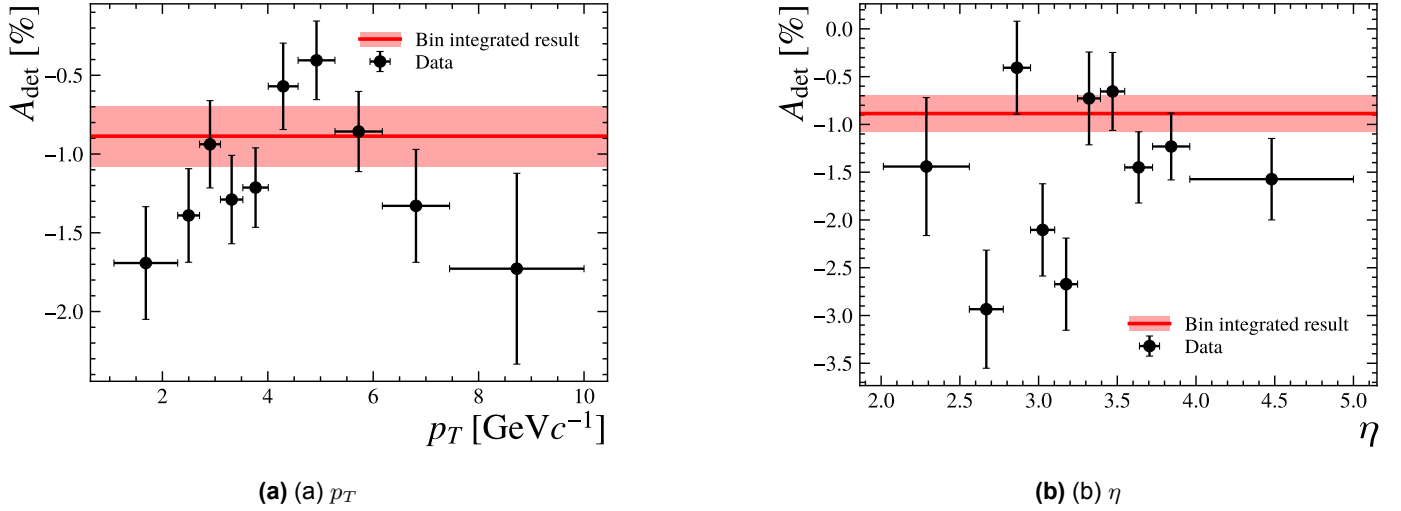

(a) (a) p_T **(b)** (b) η

Fig. 10. A kinematic dependence of detection asymmetry across the phase space for 2016 data. The data points could suggest a maximal detection asymmetry around a transverse momentum value of $5\mathrm{GeV}c^{-1}$.

7 Production Asymmetry

The production asymmetry is calculated for every combination of year and polarity using the procedure discussed in Section 2.2. The data is binned as per the scheme discussed in Section 4.2, and subsequently, a fitting procedure employing the modelling technique outlined in Section 5 is carried out for each phase-space bin. Additionally, the uncertainty calculated through quadrature does not account for systematic uncertainties. To determine the impact of such uncertainties, the following section provides a detailed outline of the relevant procedure.

Year	Bin-Integrated A_{prod} [%]	σ_{Stat} [%]	σ_{Model_Signal} [%]
2016	-0.56	$\pm$ 0.19	$\pm$ 0.01
2017	0.10	$\pm$ 0.22	$\pm$ 0.01
2018	-1.87	$\pm$ 0.22	$\pm$ 0.07
Total	-0.78	$\pm$ 0.12	$\pm$ 0.02

Table 3. A table displaying the results from the calculation of A_{prod} for each year were obtained by modelling the invariant mass distribution using Model 1.

This analysis focuses on the systematic uncertainty due to the choice of the model for the signal and is probed by using Model 1 and Model 2. The uncertainty is calculated by finding the absolute difference between the production asymmetry obtained from using Model 1 and Model 2 and is shown in Appendix D.

17

The production asymmetry is calculated for each year and polarity. Therefore, an arithmetic average was performed to compute the production asymmetry for each year individually and a pseudo-bin-integrated for all three years combined; the results are shown in Table 3. Other systematic uncertainties can be explored for future analysis, such as the uncertainty due to the choice of model for the background.

8 Pythia Simulation

Setting Types	Description	Setting
Process Level	$\sqrt{s}$ = 13TeV	`Beams:eCM = 13000`
	Momentum Spread	`Beams:AllowMomentumSpread = on`
	$gg \to \bar{c}c$	`HardQCD:gg2ccbar = on`
	$q\bar{q} \to \bar{c}c$	`HardQCD:qqbar2ccbar = on`
Parton Level	Reconnection	`ColourReconnection:mode = 1`
	Min p_T = 1GeV/c	`PhaseSpace:pTHatMin = 1`
	Max p_T = 10GeV/c	`PhaseSpace:pTHatMax = 10`
Hadron Level	Bowler modification r_c	`StringZ:rFactC = 0.67`

Table 4. A table showing the `PYTHIA` settings utilised in this analysis. These settings have been derived with slight modifications from Klaver's study of production asymmetry in D_s^+ mesons, as reported in Ref [31]. Further details regarding the settings can be found below.

This analysis simulated events using `PYTHIA 8.3`, a widely used event generator in high-energy collisions, where effects of the strong force, governed by QCD, are significant [46]. As outlined in Ref [46], the event generation process can be divided into three stages: process level, parton level, and hadron level. The process level corresponds to the hard-scattering process that can be described perturbatively using QCD. The parton level deals with showers, colour-reconnection phenomenon and beam remnants; meanwhile, the hadron level deals with hadronisation using the Lund string model described in Section 2.2.3. The physics models of hadronisation are typically non-perturbative and, therefore, require modelling and the tuning of parameters. To obtain a prediction of the D^0's production asymmetry as a function of p_T and y, a stand-alone setup of `PYTHIA` was implemented.

Most of the settings utilised in the `PYTHIA` software were kept at their default values unless otherwise specified in Table 4. To replicate the LHC beam during Run 2, the centre of mass energy was adjusted to 13 TeV, and the momentum was smoothed using a Gaussian distribution. This ensures that the simulated results correspond well with the LHCb detector's experimental observations. The HardQCD process, which is responsible for the leading order production of charm quark pairs, was simulated using the $gg \to c\bar{c}$ and $q\bar{q} \to c\bar{c}$ processes. The colour reconnection mode allows colour connection to the beam remnant, which is predicted to give asymmetry due to the beam drag effect as discussed in Section 2.2.3. Additionally, momentum selection cuts were applied to reduce the data saved, with only momentum values between 1 and 10 retained. The lower limit of 1 GeV/c corresponds to the cuts applied by LHCb's trigger, while the upper limit of 10 GeV/c is part of the selection criteria applied in this analysis, shown in Appendix A. The Lund string fragmentation is adapted using the Bowler modification for heavy quarks. The value of r_c as 0.67, as implemented by Klaver in Ref. [31], has been retained in the current analysis without any modification.

This analysis simulated 185 million events. Following the application of the selection criteria outlined in Appendix A and the removal of multiple candidates resulted in approximately 22 million events that were deemed suitable for further analysis. This is mainly due to most simulated events being outside the LHCb's acceptance range. The remaining data is split into the binning scheme used in Section 7 to compare the kinematic dependence of production asymmetry observed in simulated data and experimental observations

for each year.

9 Results and Analysis

Year	Bin-Integrated A_{prod} [%]	Bin-Integrated A_{prod}' [%]
2016	-0.56 ± 0.19 ± 0.01	-0.866 ± 0.204 ± 0.013
2017	0.10 ± 0.22 ± 0.01	-0.376 ± 0.213 ± 0.020
2018	-1.87 ± 0.22 ± 0.07	-0.397 ± 0.219 ± 0.013
Total	-0.78 ± 0.12 ± 0.02	-0.546 ± 0.122 ± 0.018

Table 5. A table showing results from calculating A_{prod} for each year that was obtained by modelling the invariant mass distribution using Model 1. The results for A_{prod}' on the right are acquired from the previous analysis.

Table 5 compares the results computed for the production asymmetry, the systematic and statistical uncertainties with those obtained by the previous analysis. The values agree for 2016, 2017, and the total pseudo-bin-integrated A_{prod}, but the statistical variation has slightly increased in some years despite the increase in the dataset. This is because the uncertainty in detection asymmetry has increased relative to previous years, as shown in Appendix A. Furthermore, the result obtained for 2018 disagrees with the prior analysis, resulting from a distinct detection asymmetry.

9.1 Kinematic Dependence
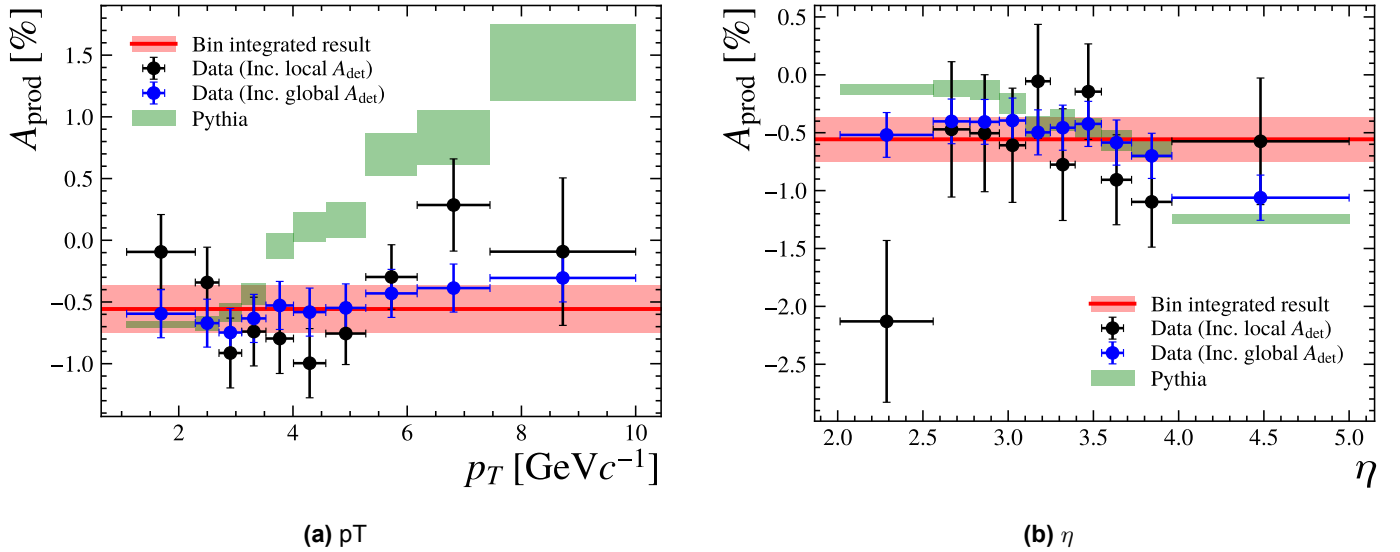

(a) pT

(b) η

Fig. 11. Graphs showing the production asymmetry in each phase-space bin. Data points are positioned at the bin centres and the horizontal uncertainties indicate the bin width.

The production asymmetry calculated in each phase-space bin is compared to asymmetry predicted from the PYTHIA simulation data using a two-sample Kolmogorov-Smirnov (KS) test. The results of the simulation are presented in Figure 11 with green rectangles, while the measured production asymmetry is represented by blue points with the global detection asymmetries, shown in Table 2, removed. Furthermore, the black points in the figure correspond to the production asymmetry where the 'local' detection asymmetries, presented in Figure 10, have been eliminated. The blue points have smaller vertical error bars than the black points due to the statistical variation of global detection asymmetry values being much smaller than the local's.

The KS test is applied twice: for comparing simulation data to the blue and black data points. The two-sample KS test is a non-parametric goodness of fit test that uses the null hypothesis that both samples come from the same distribution [47]. The KS test has the advantage of considering the distribution

functions collectively [47]. However, it is more sensitive to deviations near the distribution's centre than the tails. The KS statistic, D, is the maximum difference between the cumulative distribution function of both samples, as seen in figures in Appendix E. The D value can be compared to tabulated critical values, $D_{critical}$, for different sample sizes and significant levels. This analysis uses the value of 0.7, obtained from Ref [48], for the sample sizes of 10 at a 5% significance level. The null hypothesis can be rejected if the observed D value exceeds D_{crit}.

Parameter	Year	Data (local A_{det} removed)		Data (global A_{det} removed)	
		D	p	D	p
p_T	**2016**	0.5	16.7%	0.5	16.7%
	2017	0.5	16.7%	0.9	0.0%
	2018	0.6	5.2%	1.0	0.0%
η	**2016**	0.5	16.7%	0.6	5.2%
	2017	0.5	16.7%	0.4	41.8%
	2018	0.6	5.2%	1.0	0.0%

Table 6. A table displaying the KS statistic and p-values for the tested relationships. The p-values are found using `stats` function from SciPy [43].

Table 6 presents the D value and p-value, obtained from SciPy [43]. The results show, at a 5% significance level, the null hypothesis for half the relationships tested with data with global A_{det} removed can be rejected. Furthermore, at a 10% significance level, the total number of relationships tested that can be rejected rises to six. Therefore, based on the KS test, it is difficult to argue that the two samples come from the same distribution. This may be caused by the lack of optimisation applied to the simulation, as the `PYTHIA` simulation requires parameters to model the hadronisation.

9.2 Pythia Results

The production asymmetry calculated for the simulation's data is -0.45 ± 0.03, which is in agreement with the bin-integrated A_{prod} value for 2016. Nevertheless, the simulation can be improved. This is because the binning scheme created for the LHCb data splits the phase space into ten equally sized bins. The binning scheme, created with the collider dataset, employed in the analysis appears to fall short in its intended purpose when applied to the `PYTHIA` data. The large statistical uncertainty at high p_T bins relative to low p_T bins indicates an uneven distribution of data points across the bins. Furthermore, the beam remnant distribution function can likely cause the large positive production asymmetry observed at high p_T bins. This is because the beam drag effect, as described in Section 2.2.3, is strongly dependent on the aforementioned function, which can be subjected to modifications to model the data better.

10 Conclusions and Future Work

This report presents an analysis of the bin-integrated production asymmetry using data collected from the LHCb detector between 2016 and 2018. The report includes a calculation of the total pseudo-bin-integrated production asymmetry. The raw asymmetry is used as a probe to determine the production asymmetry through an extended maximum-likelihood fit to the IMD of the neutral D mesons. The fit is performed by representing the signal as Johnson functions and two Bifurcated Gaussian functions, and the combinatorial background is modelled using an exponential function. The detection asymmetry is calculated for each year and polarity combination. However, a key aim to reduce the statistical uncertainty of detection asymmetry could not be accomplished. The production asymmetry was computed for both polarities in each year. An arithmetic average was performed to calculate the bin-integrated result for each year and a pseudo-bin-integrated result

for the total data analysed:

$$A_{\mathsf{prod}}(D^0) = (-0.56 \pm 0.19 \pm 0.01)\% \quad (2016),$$
$$A_{\mathsf{prod}}(D^0) = (\ \ 0.10 \pm 0.22 \pm 0.01)\% \quad (2017),$$
$$A_{\mathsf{prod}}(D^0) = (-1.87 \pm 0.22 \pm 0.07)\% \quad (2018),$$
$$A_{\mathsf{prod}}(D^0) = (-0.78 \pm 0.12 \pm 0.02)\% \quad (\mathsf{Total}),$$

where the first uncertainty is statistical and the second is systematic uncertainty. Compared to the previous analysis, the values agree for 2016, 2017, and the total pseudo-bin-integrated A_{prod}. However, the 2018 result does not agree due to the different detection asymmetry values used.

The analysis successfully quadrupled the dataset's size, reducing the raw asymmetry statistical uncertainty. However, due to limited memory capacity, only a million events were employed in the reweighting process, resulting in substantial statistical uncertainty for the detection asymmetry. Furthermore, a clear kinematic correlation for detection asymmetry could not be established due to significant Poisson uncertainties in the phase-space bins. The PYTHIA simulation was employed in the analysis to compare measured production asymmetries with simulated results. However, based on the KS test, it is difficult to confidently state that both samples originate from the same distribution. Future analyses may benefit from optimising the beam remnant distribution and Bowler modification to address this issue.

Future analysis requires calculating detection asymmetry involving a larger dataset to find a more definitive result for the detection and production asymmetries and the kinematic relationships. The PYTHIA simulation can be improved by optimising parameters. Another effective approach to studying the kinematic distribution is to utilise QCD calculation, wherein non-perturbative parameters can be fitted, as explained in Ref. [12].

References

[1] The LHCb Collaboration, "The LHCb Detector at the LHC," *Journal of Instrumentation*, vol. 3, no. 08, 2008.

[2] R. Gauld and et al., "Beauty-quark and charm-quark pair production asymmetries at LHCb," *Phys. Rev. D*, vol. 92, p. 034 007, 3 2015.

[3] S. Stemmle, "Measurement of the time-integrated CP asymmetry in prompt $D^0 \rightarrow K^- K^+$ decays with the LHCb experiment," Master's thesis, University of Heidelberg, 2015.

[4] L. Seelan, "Measurement of the production asymmetry between $\bar{D}^0$ and D^0 mesons in proton-proton collisions at the lhcb experiment," Master's thesis, University of Manchester, 2024.

[5] G. Altarelli and J. Wells, "Gauge Theories and the Standard Model," in *Collider Physics within the Standard Model* (Lecture Notes in Physics), Lecture Notes in Physics. Springer, 2017, vol. 937.

[6] E. Kennedy, "The Generation Model of Particle Physics," in *Particle Physics*. IntechOpen, 2012.

[7] W. N. Cottingham, *An Introduction to the Standard Model of Particle Physics*, 2nd ed. Cambridge University Press, 2023.

[8] S. Chatrchyan and et al, "Observation of a new boson at a mass of 125 GeV with the CMS experiment at the LHC," *Physics Letters B*, vol. 716, no. 1, pp. 30–61, 2012.

[9] D. Boer, *Gluons and the quark sea at high energies: distributions, polarization, tomography*, 2011. arXiv: `1108.1713 [nucl-th]`.

[10] C. Avila, *Charm particle production in hadronic collisions*, 2006. arXiv: `hep-ph/0307358 [hep-ph]`.

[11] B. R. Martin and G. Shaw, *Particle Physics*, 4th ed. Wiley, 2016.

[12] W. Lai and et.al, "Production Asymmetry at the LHC from heavy quark recombination," *Phys. Rev. D*, vol. 90, no. 5, 2014.

[13] E. Braaten, Y. Jia, and T. Mehen, "Leading-Particle Effect from Heavy-Quark Recombination," *Phys. Rev. Lett.*, vol. 89, p. 122 002, 12 2002.

[14] J. C. Collins, D. E. Soper, and G. Sterman, "Heavy particle production in high-energy hadron collisions," *Nuclear Physics B*, vol. 263, no. 1, pp. 37–60, 1986.

[15] R. Aaij and et.al, "Measurement of the $D^{\pm}$ production asymmetry in 7 TeV pp collisions," *Physics Letters B*, vol. 718, no. 3, pp. 902–909, 2013.

[16] R. Aaij, "Measurement of CP asymmetry in $D^0 \to K^- K^+$ and $D^0 \to \pi^- \pi^+$ decays," *Journal of High Energy Physics*, vol. 2014, no. 7, 2014.

[17] J. Bernabeu, "Discrete Symmetries CP, T, CPT," *Journal of Physics: Conference Series*, vol. 631, no. 1, p. 012 015, 2015.

[18] T. Gershon, "CP violation in the B system," *Reports on Progress in Physics*, vol. 80, no. 4, 2017.

[19] R. L. Workman and et al., "Review of Particle Physics," *Progress of Theoretical and Experimental Physics*, vol. 2022, no. 8, p. 083C01, 2022.

[20] C. Peterson and et al., "Scaling Violations in Inclusive e+ e- Annihilation Spectra," *Phys. Rev. D*, 1983.

[21] E. Braaten and et al., "B production asymmetries in perturbative QCD," *Phys. Rev. D*, vol. 66, 3 2002.

[22] S. Forte and S. Carrazza, *Parton distribution functions*, 2020. arXiv: `2008.12305 [hep-ph]`.

[23] A. Petrukhin, "Measurements of the proton structure at HERA and their impact for LHC," *Nuclear Physics B - Proceedings Supplements*, vol. 207–208, pp. 45–48, 2010.

[24] R. Vogt, "Heavy flavor azimuthal correlations in cold nuclear matter," *Physical Review C*, vol. 98, 2018.

[25] L. M. Kashif, "Measurement of the Z boson cross-section in the dimuon channel in pp collisions at $\sqrt{s} =$ 7 TeV," PhD Dissertation, Harvard University, 2010.

[26] E. Braaten, Y. Jia, and T. Mehen, "Charm-anticharm asymmetries in photoproduction from heavy-quark recombination," *Phys. Rev. D*, vol. 66, 1 2002.

[27] M. Petricean, "Probing Strangeness Production in Proton-Proton Collisions with Three-Particle Correlations," PhD Dissertation, Lund University, 2023.

[28] Norrbin, E. and et al., "Production and hadronization of heavy quarks," *The European Physical Journal C - Particles and Fields*, vol. 17, no. 1, pp. 137–161, 2000.

[29] E. Norrbin and T. Sjöstrand, "Production mechanisms of charm hadrons in the string model," *Physics Letters B*, vol. 442, no. 1–4, pp. 407–416, 1998.

[30] E. Norrbin, *Heavy Quark Production Asymmetries*, 1999. arXiv: `hep-ph/9909437 [hep-ph]`.

[31] S. Klaver, "Measurements of CP violation in mixing of B_s^0 mesons and the D_s^+ production asymmetry at LHCb," PhD Dissertation, University of Manchester, 2017.

[32] Y. Bi, H. Cai, Y. Chen, *et al.*, "Diquark mass differences from unquenched lattice QCD," *Chinese Physics C*, vol. 40, no. 7, p. 073 106, 2016.

[33] M.Yu. Barabanov and et al., "Diquark correlations in hadron physics: Origin, impact and evidence," *Progress in Particle and Nuclear Physics*, vol. 116, p. 103 835, 2021.

[34] S. Prestel, "Recent developments in the Pythia event generator," PowerPoint presentation, 2018.

[35] F. D. Lorenzi, "Parton Distribution Function Studies and a Measurement of Drell-Yan Produced Muon Pairs at LHCb ," PhD Dissertation, University College Dublin, 2011.

[36] The LHCb Collaboration, "LHCb detector performance," *International Journal of Modern Physics A*, vol. 30, no. 07, 2015.

[37] B. Quintana, "Particle identification of neutral particles at LHCb," *PoS*, vol. LHCP2018, p. 046, 2018.

[38] J. J. van Hunen, "The LHCb tracking system," *Nuclear Instruments and Methods in Physics Research Section A*, vol. 572, no. 1, pp. 149–153, 2007.

[39] R. Kopecna, "Tracking and vertexing in LHCb," *PoS*, vol. VERTEX2018, p. 039, 2019.

[40] J. Albrecht, "The LHCb Trigger System," *Nucl. Phys. B, Proc. Suppl.*, vol. 187, pp. 237–244, 2009.

[41] T. Head, "The LHCb trigger system," *JINST*, vol. 9, p. C09015, 2014.

[42] W. Verkerke and D. P. Kirkby, "The RooFit toolkit for data modeling," 2003. arXiv: `physics/0306116`.

[43] P. Virtanen, "SciPy 1.0: Fundamental Algorithms for Scientific Computing in Python," *Nature Methods*, vol. 17, pp. 261–272, 2020.

[44] The LHCb Collaboration, "Measurement of the $B^\pm$ production asymmetry and the CP asymmetry in $B^\pm \to J/\psi K^\pm$ decays," *Phys. Rev. D*, vol. 95, no. 5, p. 052 005, 2017.

[45] A. Davis and et al., "Measurement of the instrumental asymmetry for $K^-\pi^+$-pairs at LHCb in Run 2," CERN, Geneva, Tech. Rep., 2018.

[46] C. B. and et al., *A comprehensive guide to the physics and usage of PYTHIA 8.3*, 2022. arXiv: `2203.11601 [hep-ph]`.

[47] Y. Dodge, "Kolmogorov–Smirnov Test," in *The Concise Encyclopedia of Statistics*. New York, NY: Springer New York, 2008, pp. 283–287.

[48] F. J. Rohlf and R. R. Sokal, *Statistical tables*, 2nd ed. Oxford: W.H. Freeman, 1981.

[49] C. Jarvis-Stiggants, "Measurement of the $\bar{D}^0 - D^0$ production asymmetry in pp collisions at $\sqrt{s} = 13$ TeV," Master's thesis, University of Manchester, 2023.

Appendices

A Previous Analysis

A.1 Selection

Variable	Requirement
PID of particle 1	Not a muon
PID of particle 2	Not a muon
$\eta(D^0)$	$[2,5]$
$p_z(K)$	> 0
$p_z(\pi)$	> 0
$p_T(D^0)$	$[0,10]$ GeVc^{-1}
$\ln \chi^2_{IP}$	< 1.2
πDLL$_{K-\pi}$	< 0
KDLL$_{K-\pi}$	> 5

Table 7. The selection criteria applied proposed in the prior analysis by Camille Jarvis-Stiggants and Micheal England. Further details are in Ref. [49].

A.2 Detection Asymmetry from Previous Analysis

		$A_{det}(K^-\pi^+)$ [%]	
Model	**Polarity**	**Previous Analysis**	**Current Analysis**
2016	MagUp	-0.82 ± 0.26	-1.95 ± 0.29
	MagDown	-0.10 ± 0.25	0.39 ± 0.25
2017	MagUp	-0.76 ± 0.27	-2.75 ± 0.31
	MagDown	-0.99 ± 0.27	-0.07 ± 0.32
2018	MagUp	-0.25 ± 0.27	-0.02 ± 0.31
	MagDown	-0.97 ± 0.28	-1.27 ± 0.32

Table 8. A table comparing the detection asymmetry obtained from the previous analysis and this analysis.

B Modelling

	Previous Analysis		Current Analysis	
Model	μ	σ	μ	σ
Model 1	-0.11 ± 0.05	1.23 ± 0.10	-0.25 ± 0.04	1.72 ± 0.04
Model 2	-0.08 ± 0.26	1.27 ± 0.26	-0.11 ± 0.24	2.37 ± 0.29

Table 9. Comparison of the mean and standard deviation values obtained from fitting a Gaussian to the pull distribution for each model between the prior and current analysis.

B.1 Model 1

Year	Meson	Polarity	μ	σ
2016	D0	MagUp	-0.25 ± 0.12	1.56 ± 0.12
		MagDown	-0.52 ± 0.11	1.62 ± 0.11
	D0bar	MagUp	-0.23 ± 0.17	1.83 ± 0.17
		MagDown	-0.31 ± 0.09	1.58 ± 0.09
2017	D0	MagUp	-0.20 ± 0.11	1.62 ± 0.11
		MagDown	-0.15 ± 0.13	1.95 ± 0.13
	D0bar	MagUp	-0.06 ± 0.11	1.57 ± 0.11
		MagDown	-0.12 ± 0.16	1.80 ± 0.16
2018	D0	MagUp	-0.29 ± 0.11	1.85 ± 0.11
		MagDown	-0.37 ± 0.12	1.63 ± 0.12
	D0bar	MagUp	-0.17 ± 0.14	1.63 ± 0.14
		MagDown	-0.27 ± 0.13	1.95 ± 0.13
Average			−0.25 ± 0.04	1.72 ± 0.04

Table 10. Table showing the μ and σ of the pull distribution for each year, and polarity obtained by modelling the invariant mass distribution using a binned fit of Model 1.

B.2 Model 2

Year	Meson	Polarity	μ	σ
2016	D0	MagUp	-0.45 ± 0.12	1.92 ± 0.13
		MagDown	-0.04 ± 0.12	1.81 ± 0.13
	D0bar	MagUp	-0.34 ± 0.19	2.03 ± 0.20
		MagDown	-0.28 ± 0.17	2.17 ± 0.17
2017	D0	MagUp	-0.01 ± 0.22	2.24 ± 0.23
		MagDown	-0.11 ± 0.13	2.02 ± 0.13
	D0bar	MagUp	-0.54 ± 0.20	2.34 ± 0.21
		MagDown	-0.11 ± 0.19	2.49 ± 0.20
2018	D0	MagUp	0.68 ± 0.63	2.50 ± 0.85
		MagDown	0.39 ± 0.34	3.15 ± 0.42
	D0bar	MagUp	-0.30 ± 0.32	3.10 ± 0.40
		MagDown	-0.26 ± 0.32	2.71 ± 0.43
Average			-0.11 ± 0.24	2.37 ± 0.29

Table 11. Table showing the μ and σ of the pull distribution for each year, and polarity obtained by modelling the invariant mass distribution using a binned fit of Model 2.
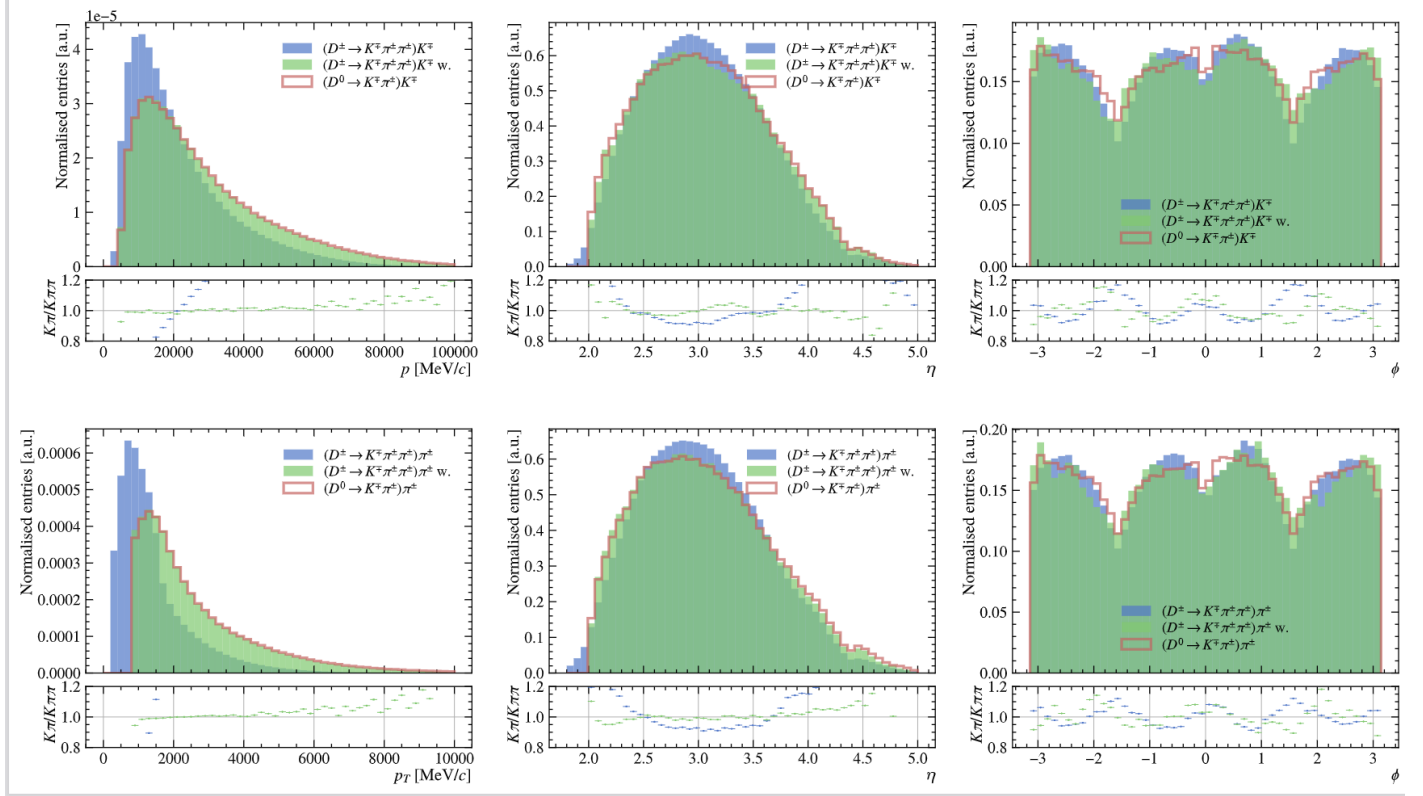
C Detection Asymmetry

Fig. 12. The reweighted kinematic distributions of (p, η, ϕ) and (p_T, η, ϕ) for the $D^\pm \to K^\mp \pi^\pm \pi^\pm$ control mode using the 2017 MagDown dataset. The ratios of control mode over the desired kinematic regime are also shown in the graph.
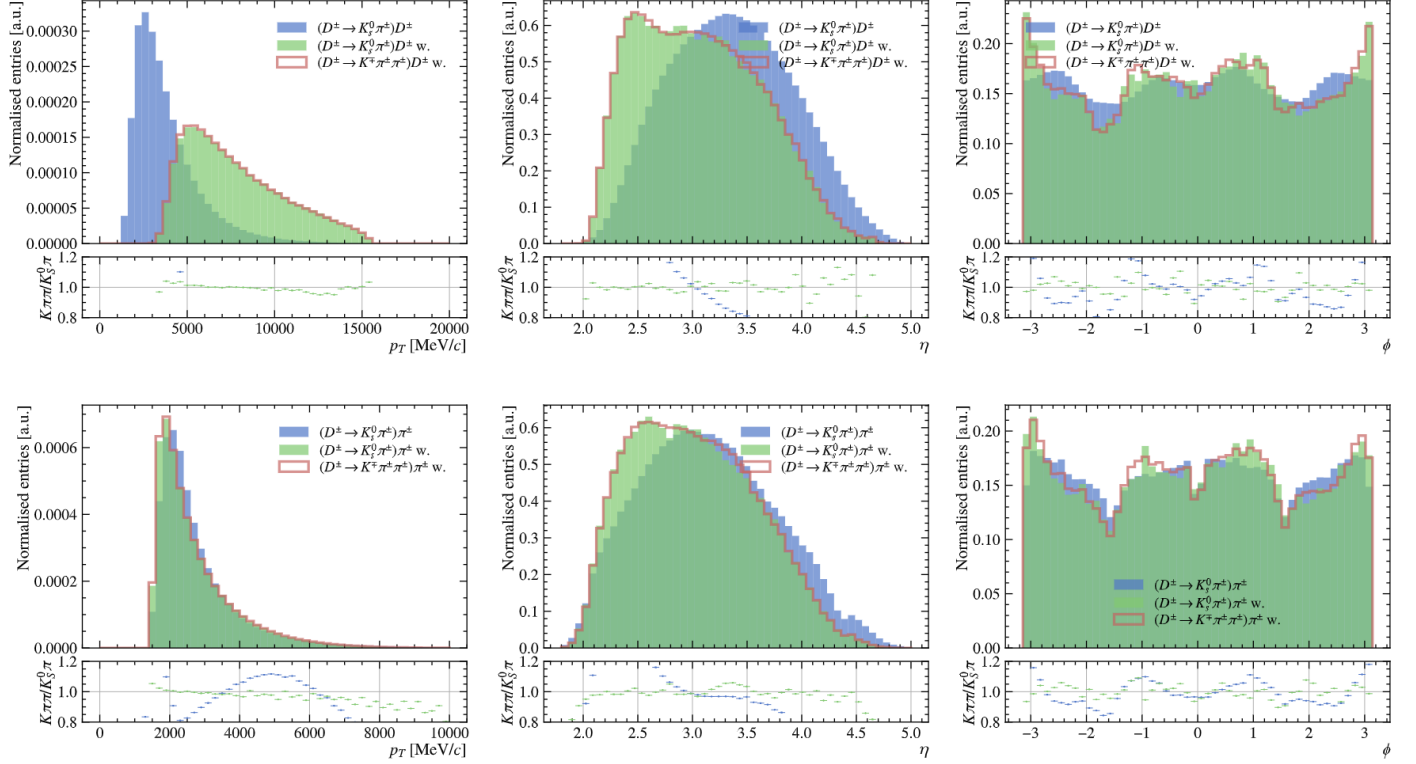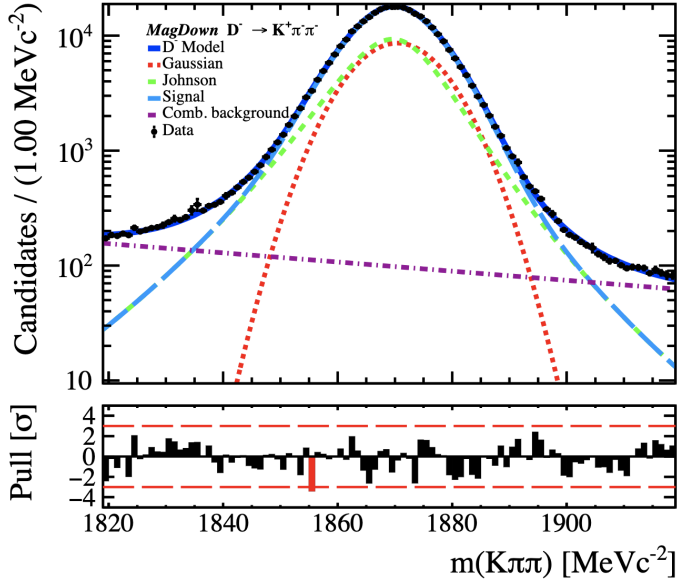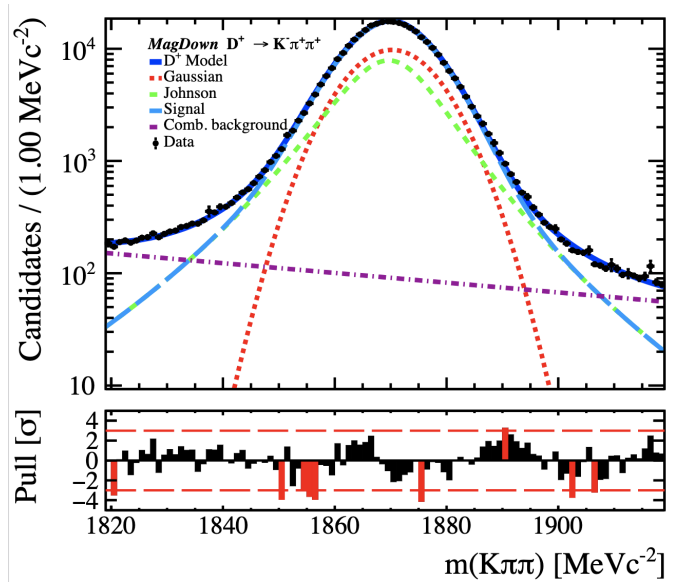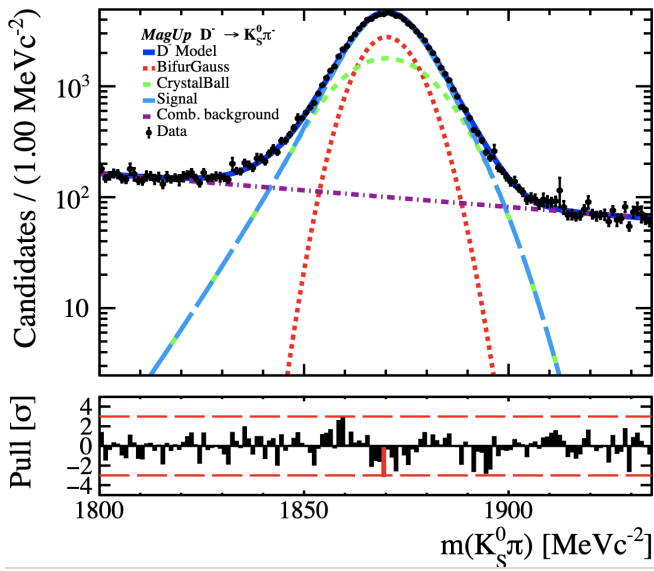

Fig. 13. The reweighted kinematic distributions of (p, η, ϕ) and (p_T, η, ϕ) for the $D^\pm \to K_s^0 \pi^\pm$ control mode using the 2017 MagDown dataset. The ratios of control mode over the desired kinematic regime are also shown in the graph.

C.1 Modelling control modes

(a) 2016 MagDown $K\pi\pi$

(b) 2016 MagDown $K\pi\pi$

Fig. 14. Graphs showing the invariant mass distribution of $K\pi\pi$ after the reweighting procedure.

(a) 2016 MagUp $K_s\pi$
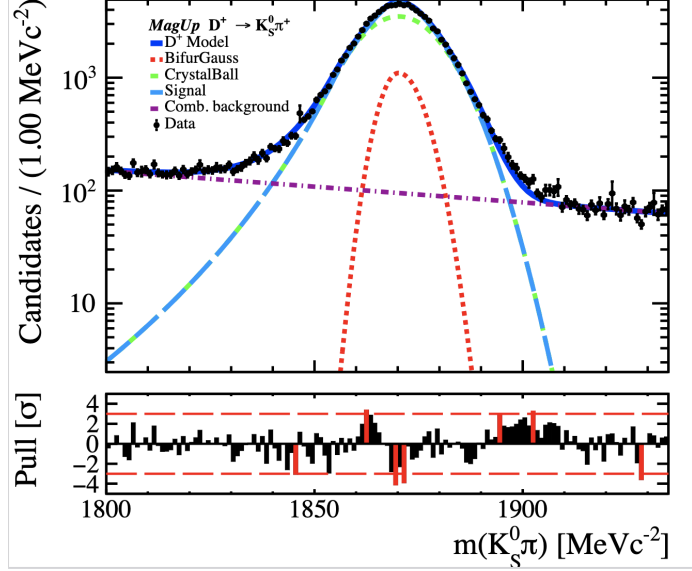
(b) 2016 MagUp $K\pi\pi$

Fig. 15. Graphs showing the invariant mass distribution of $K_s\pi$ after the reweighting procedure.

27

C.2 Local Detection Asymmetry

C.2.1 p_T

p_T bin	$A_{det}(K^-\pi^+)$ [%]	$\sigma_{A_{det}}$ [%]
0	-0.867	0.323
1	-0.826	0.381
2	-0.287	0.400
3	-0.055	0.382
4	0.192	0.433
5	-0.159	0.397
6	-0.737	0.349
7	-0.966	0.370
8	-1.574	0.543
9	0.192	0.433

Table 12. The 2016 *MagDown* detection asymmetries in the p_T binning scheme.

p_T bin	$A_{det}(K^-\pi^+)$ [%]	$\sigma_{A_{det}}$ [%]
0	-0.867	0.323
1	-0.826	0.381
2	-0.287	0.400
3	-0.055	0.382
4	0.192	0.433
5	-0.159	0.397
6	-0.737	0.349
7	-0.966	0.370
8	-1.574	0.543
9	-0.255	0.829

Table 13. The 2016 *MagUp* detection asymmetries in the p_T binning scheme.

p_T bin	$A_{det}(K^-\pi^+)$ [%]	$\sigma_{A_{det}}$ [%]
0	-1.186	0.307
1	-1.262	0.338
2	-0.208	0.316
3	-0.413	0.361
4	-1.303	0.376
5	-1.128	0.402
6	-0.781	0.363
7	-0.272	0.413
8	0.908	0.727
9	-0.099	0.895

Table 14. The 2017 *MagDown* detection asymmetries in the p_T binning scheme.

p_T **bin**	$A_{det}(K^-\pi^+)$ **[%]**	$\sigma_{A_{det}}$ **[%]**
0	-0.772	0.288
1	-0.661	0.326
2	-1.108	0.315
3	-0.756	0.314
4	0.060	0.377
5	-0.802	0.424
6	-0.982	0.368
7	-1.440	0.413
8	-2.274	0.477
9	-2.766	0.881

Table 15. The 2017 *MagUp* detection asymmetries in the p_T binning scheme.

p_T **bin**	$A_{det}(K^-\pi^+)$ **[%]**	$\sigma_{A_{det}}$ **[%]**
0	-0.590	0.377
1	-0.964	0.309
2	-0.072	0.335
3	-0.874	0.344
4	-0.633	0.360
5	-0.247	0.363
6	-0.388	0.456
7	-0.806	0.548
8	-1.778	0.512
9	0.302	0.923

Table 16. The 2018 *MagDown* detection asymmetries in the p_T binning scheme.

p_T **bin**	$A_{det}(K^-\pi^+)$ **[%]**	$\sigma_{A_{det}}$ **[%]**
0	-1.046	0.417
1	-1.874	0.333
2	-1.040	0.303
3	-0.740	0.336
4	-0.548	0.345
5	-0.479	0.342
6	-0.416	0.317
7	-0.596	0.388
8	-1.108	0.506
9	-0.379	1.192

Table 17. The 2018 *MagUp* detection asymmetries in the p_T binning scheme.

C.2.2 η

η bin	$A_{det}(K^-\pi^+)$ [%]	$\sigma_{A_{det}}$ [%]
0	2.889	0.952
1	1.299	0.774
2	-1.17	0.736
3	0.758	0.708
4	0.016	0.703
5	-0.407	0.673
6	-1.675	0.584
7	0.320	0.565
8	0.253	0.599
9	-1.174	0.908

Table 18. The 2016 *MagDown* detection asymmetries in the η binning scheme.

η bin	$A_{det}(K^-\pi^+)$ [%]	$\sigma_{A_{det}}$ [%]
0	-1.441	1.021
1	-2.934	0.874
2	-0.407	0.689
3	-2.104	0.683
4	-2.672	0.682
5	-0.728	0.687
6	-0.655	0.577
7	-1.450	0.527
8	-1.231	0.495
9	-1.573	0.603

Table 19. The 2016 *MagUp* detection asymmetries in the η binning scheme.

η bin	$A_{det}(K^-\pi^+)$ [%]	$\sigma_{A_{det}}$ [%]
0	-4.054	1.116
1	-1.094	0.684
2	-2.446	0.623
3	-0.291	0.659
4	2.516	0.769
5	-1.337	0.698
6	-3.533	0.703
7	-2.538	0.513
8	0.648	0.713
9	0.321	0.801

Table 20. The 2017 *MagDown* detection asymmetries in the η binning scheme.

η bin	$A_{det}(K^-\pi^+)$ [%]	$\sigma_{A_{det}}$ [%]
0	-3.884	1.053
1	0.083	1.304
2	-1.803	0.632
3	-1.37	0.584
4	-1.311	0.633
5	-3.963	0.785
6	-1.864	0.685
7	−1.399	0.58
8	-2.935	0.506
9	-0.146	0.705

Table 21. The 2017 *MagUp* detection asymmetries in the η binning scheme.

η bin	$A_{det}(K^-\pi^+)$ [%]	$\sigma_{A_{det}}$ [%]
0	2.220	1.514
1	-1.737	0.689
2	0.780	0.633
3	3.283	0.609
4	0.995	0.707
5	-0.193	0.670
6	-0.095	0.690
7	-1.259	0.592
8	-1.094	0.571
9	0.326	0.784

Table 22. The 2018 *MagDown* detection asymmetries in the η binning scheme.

η bin	$A_{det}(K^-\pi^+)$ [%]	$\sigma_{A_{det}}$ [%]
0	-0.703	1.112
1	-2.063	0.661
2	-0.027	0.584
3	-1.099	0.611
4	-1.372	0.676
5	2.220	0.648
6	0.145	0.627
7	0.335	0.594
8	-2.235	0.656
9	-0.584	0.638

Table 23. The 2018 *MagUp* detection asymmetries in the η binning scheme.

D Systematic Uncertainty

Year	Integrated A_{prod} [%]	Integrated A_{prod}' [%]	σ_{Fit}
2016	-0.56 $\pm$ 0.19	-0.57 $\pm$ 0.19	0.01
2017	0.10 $\pm$ 0.22	0.09 $\pm$ 0.22	0.01
2018	-1.87 $\pm$ 0.22	-1.94 $\pm$ 0.22	0.07

Table 24. Results from calculating A_{prod} and A_{prod}' for each year obtained by modelling the invariant mass distribution using Model 1 and Model 2, respectively. The difference between the two asymmetries yields the systematic uncertainty for the model.

E Kolmogorov-Smirnov test
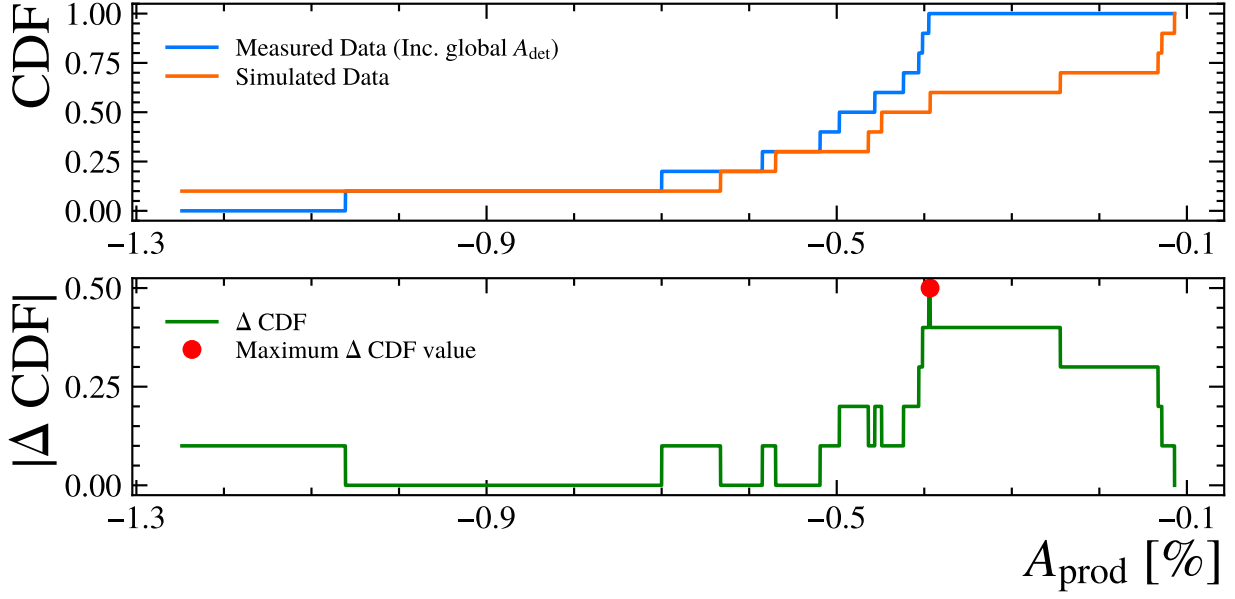
Fig. 16. A cumulative distribution function for the production asymmetry with global detection asymmetry removed in 2016 η phase-space bin and the simulated data. The maximum difference between the two CDFs is also plotted.
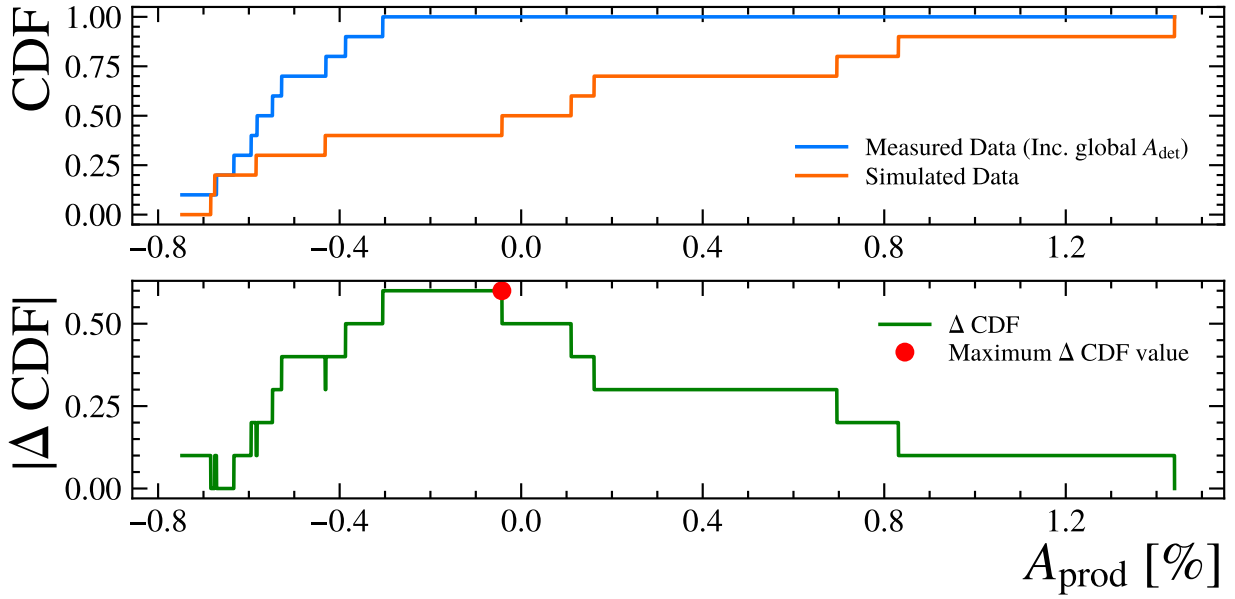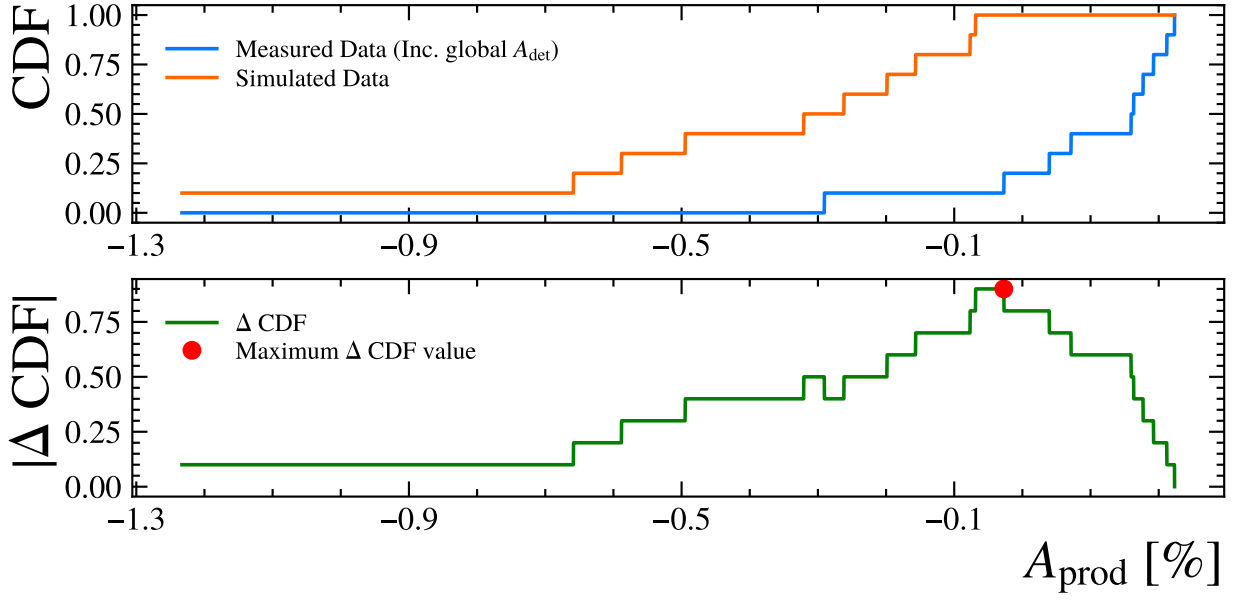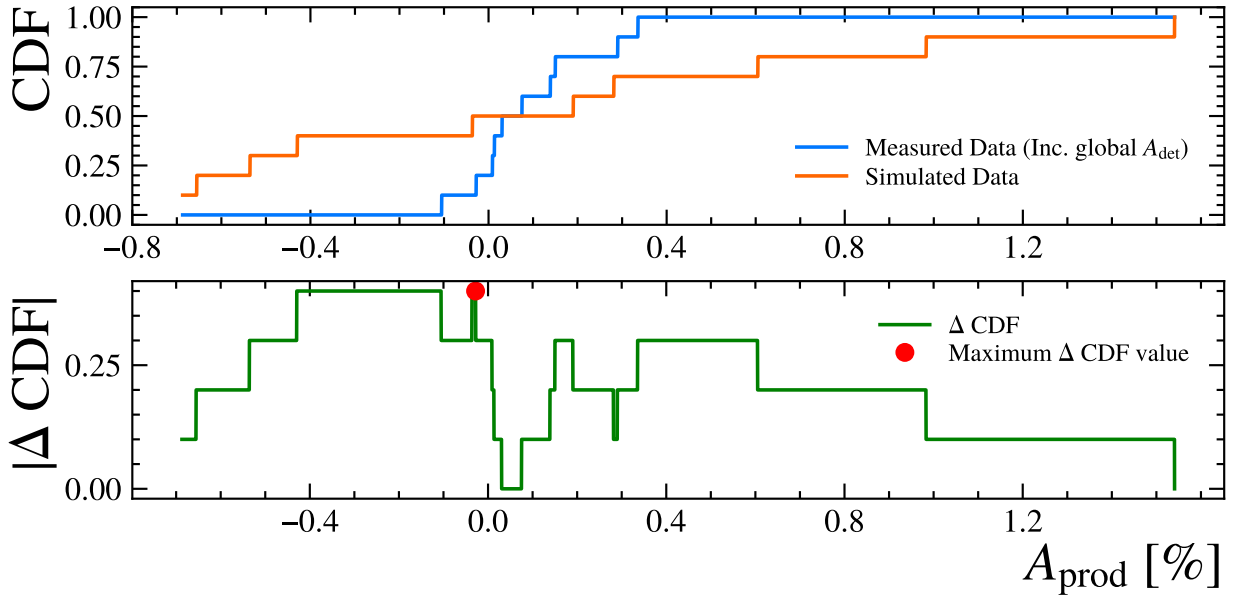

Fig. 17. A cumulative distribution function for the production asymmetry with global detection asymmetry removed in 2016 pT phase-space bin and the simulated data. The maximum difference between the two CDFs is also plotted.
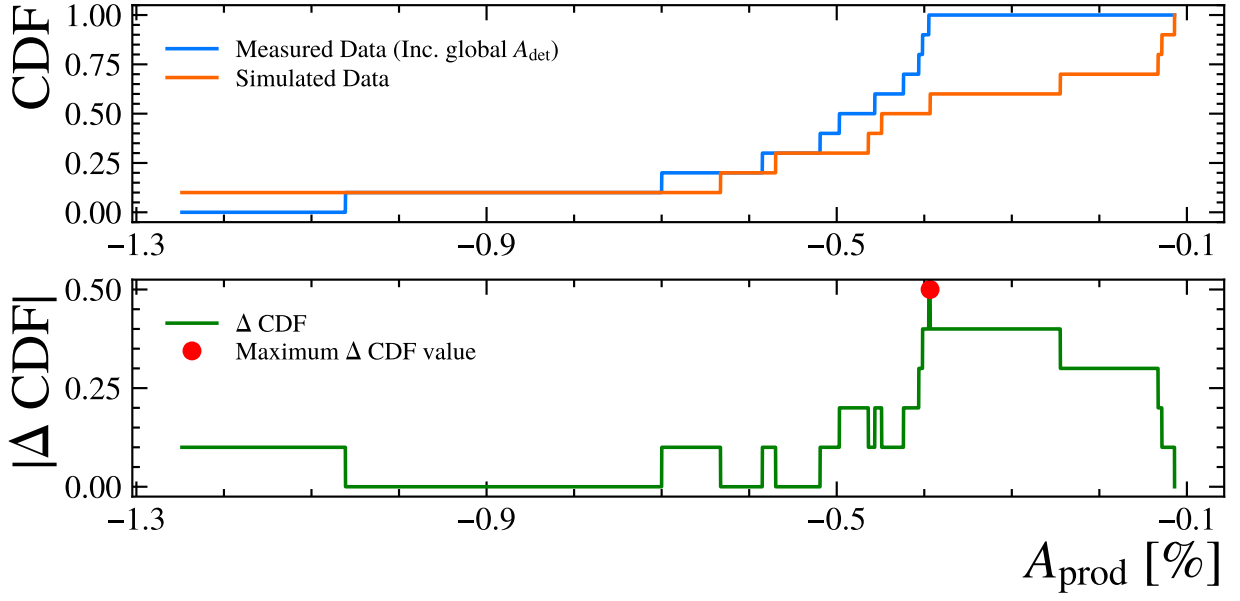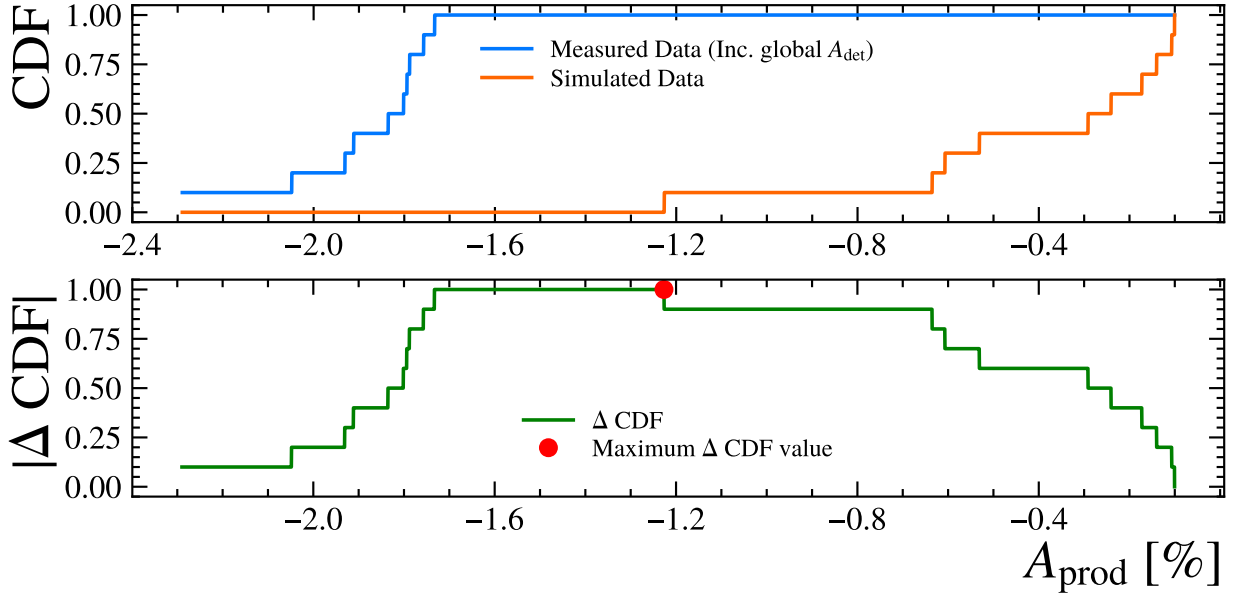
Fig. 18. A cumulative distribution function for the production asymmetry with local detection asymmetry removed in 2016 η phase-space bin and the simulated data. The maximum difference between the two CDFs is also plotted.
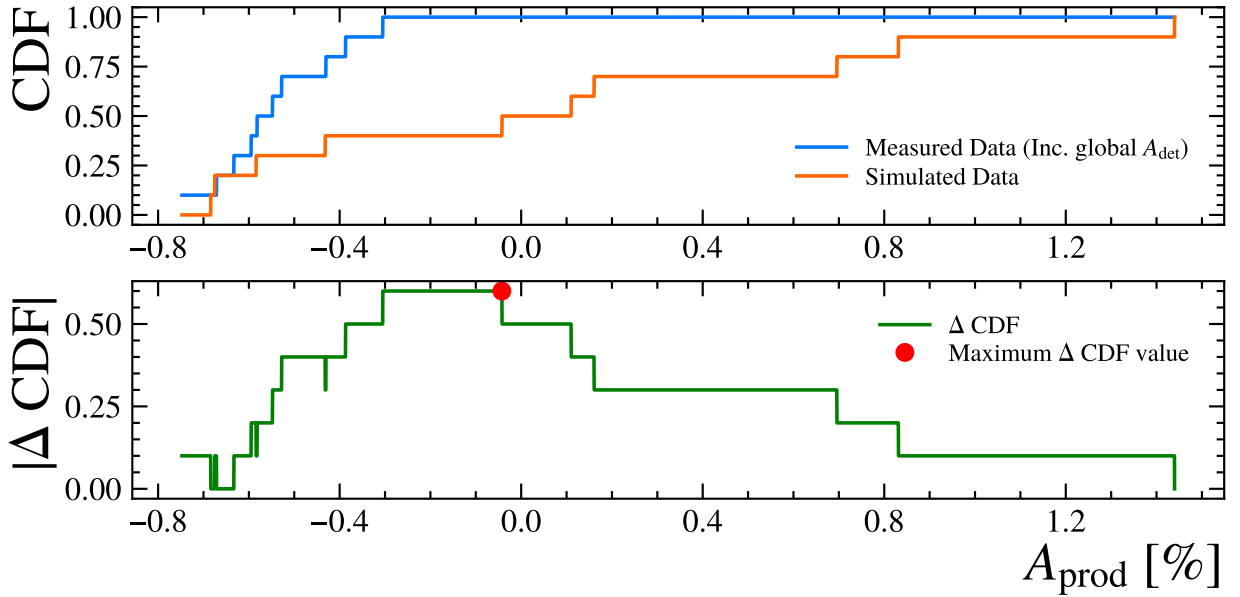
Fig. 19. A cumulative distribution function for the production asymmetry with local detection asymmetry removed in 2016 pT phase-space bin and the simulated data. The maximum difference between the two CDFs is also plotted.
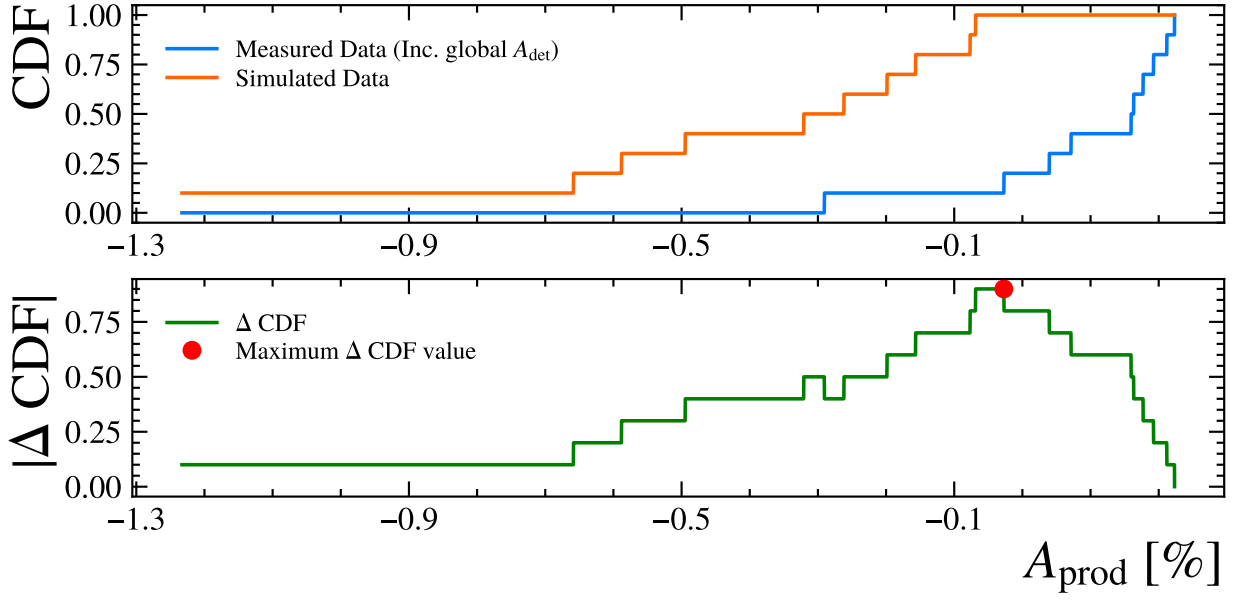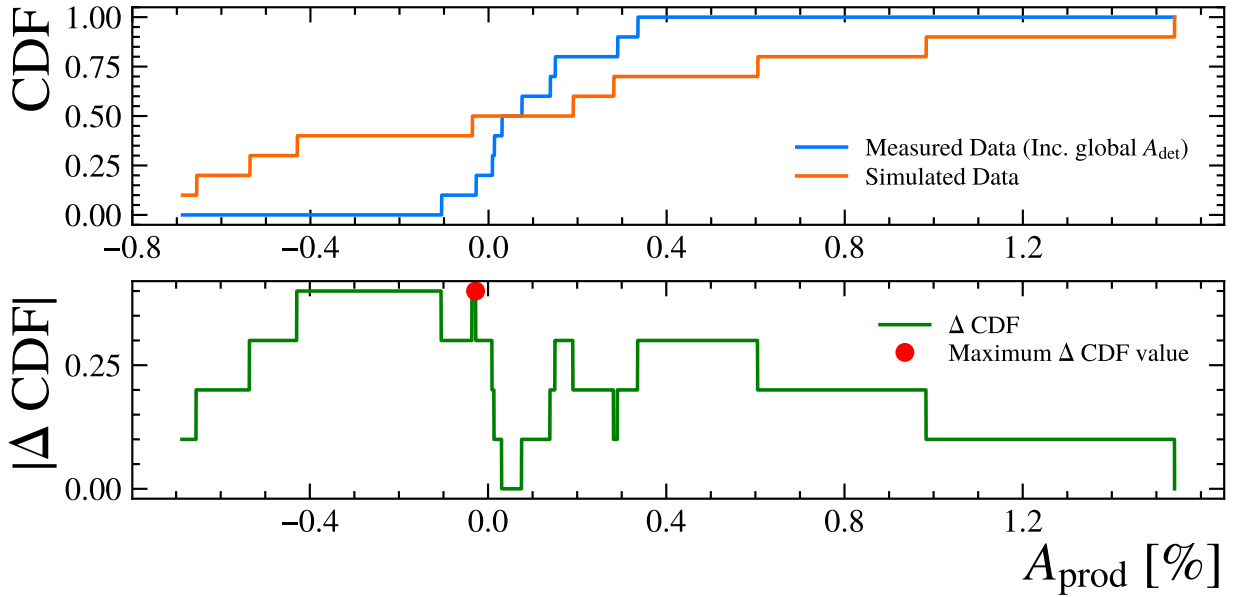
Fig. 20. A cumulative distribution function for the production asymmetry with global detection asymmetry removed in 2017 η phase-space bin and the simulated data. The maximum difference between the two CDFs is also plotted.
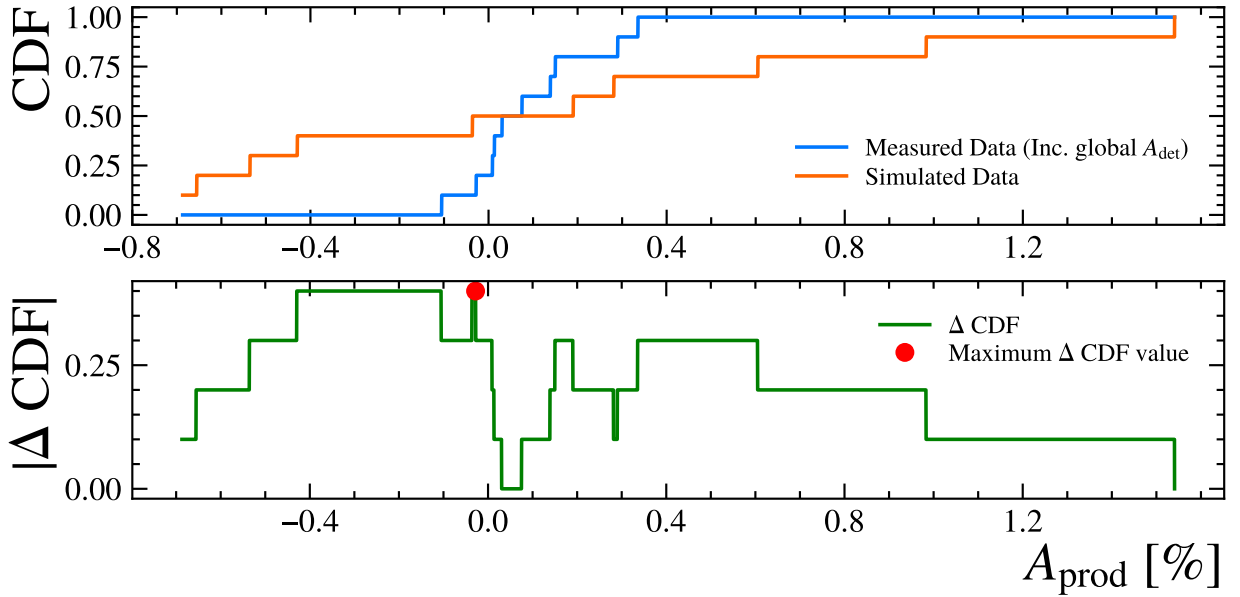
Fig. 21. A cumulative distribution function for the production asymmetry with global detection asymmetry removed in 2017 pT phase-space bin and the simulated data. The maximum difference between the two CDFs is also plotted.
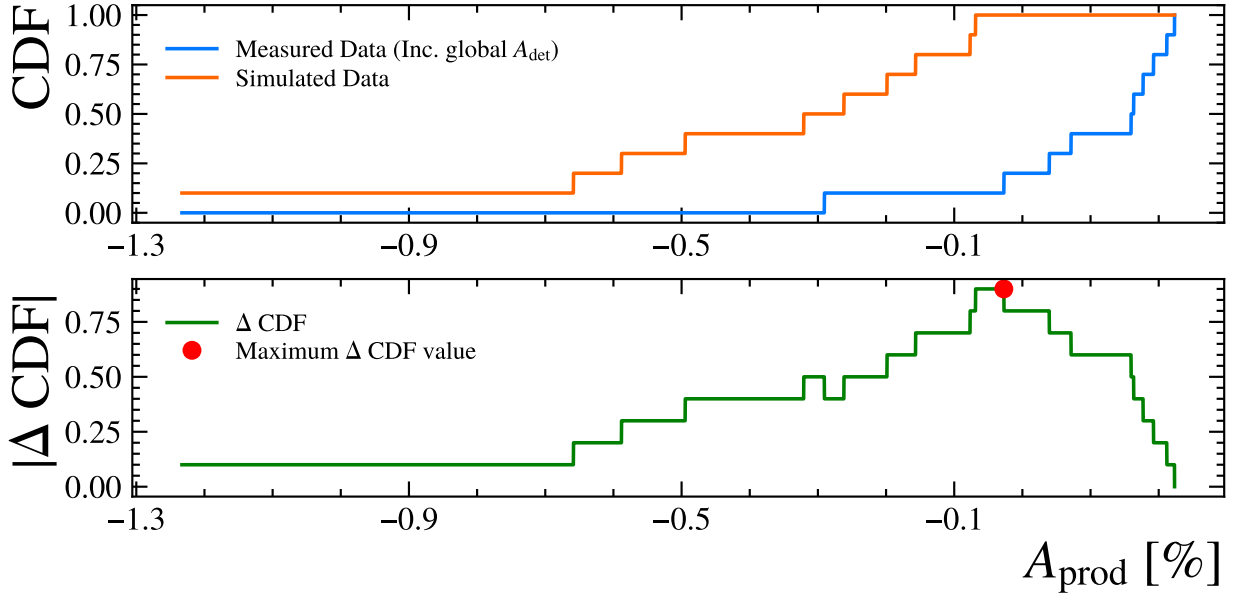
Fig. 22. A cumulative distribution function for the production asymmetry with local detection asymmetry removed in 2017 η phase-space bin and the simulated data. The maximum difference between the two CDFs is also plotted.
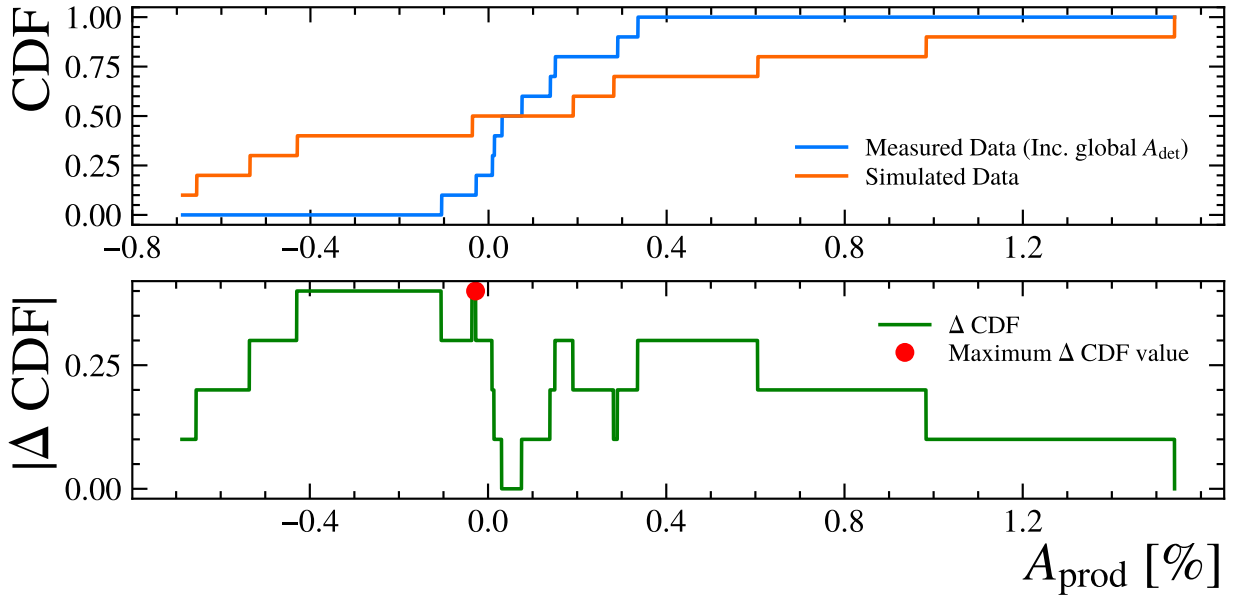

Fig. 23. A cumulative distribution function for the production asymmetry with local detection asymmetry removed in 2017 pT phase-space bin and the simulated data. The maximum difference between the two CDFs is also plotted.

Fig. 24. A cumulative distribution function for the production asymmetry with global detection asymmetry removed in 2018 η phase-space bin and the simulated data. The maximum difference between the two CDFs is also plotted.


Fig. 25. A cumulative distribution function for the production asymmetry with global detection asymmetry removed in 2018 pT phase-space bin and the simulated data. The maximum difference between the two CDFs is also plotted.

Fig. 26. A cumulative distribution function for the production asymmetry with local detection asymmetry removed in 2018 η phase-space bin and the simulated data. The maximum difference between the two CDFs is also plotted.

Fig. 27. A cumulative distribution function for the production asymmetry with local detection asymmetry removed in 2018 pT phase-space bin and the simulated data. The maximum difference between the two CDFs is also plotted.

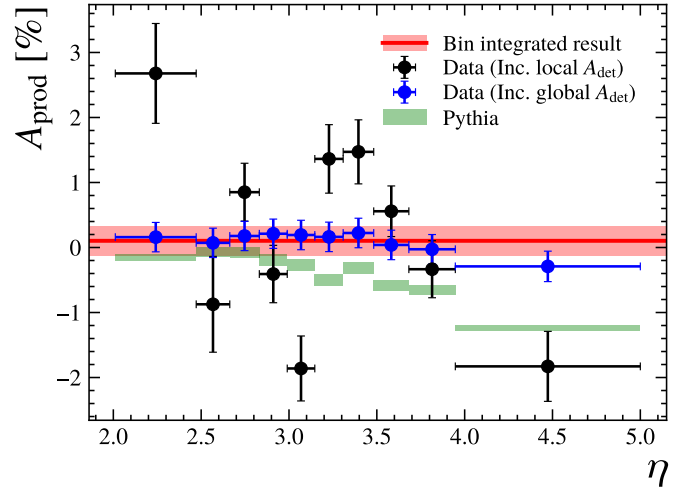# F Kinematic Dependency

(a) 16 p_T

(b) 16 η
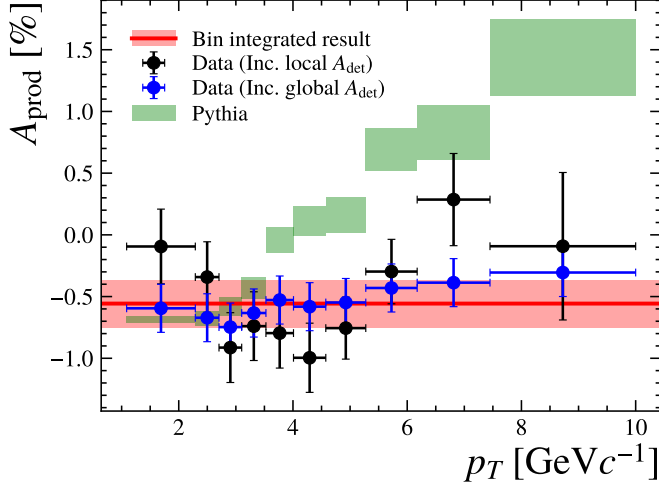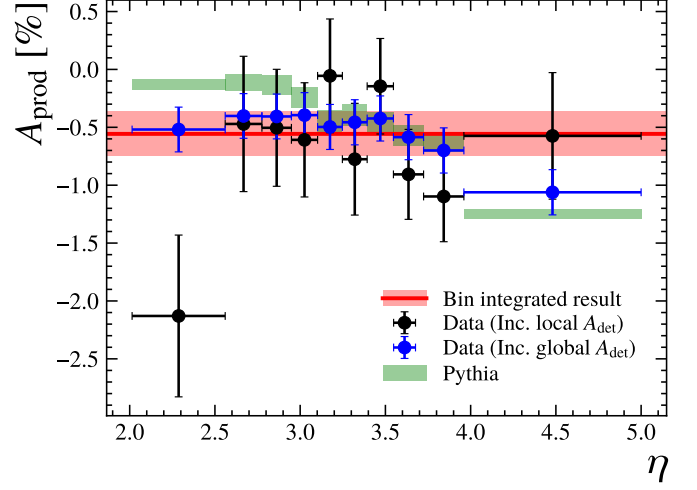
Fig. 28. Graphs showing the production asymmetry in each phase-space bin. The value for the kinematic variable is found by calculating the bin centre, and its error is half the bin width.
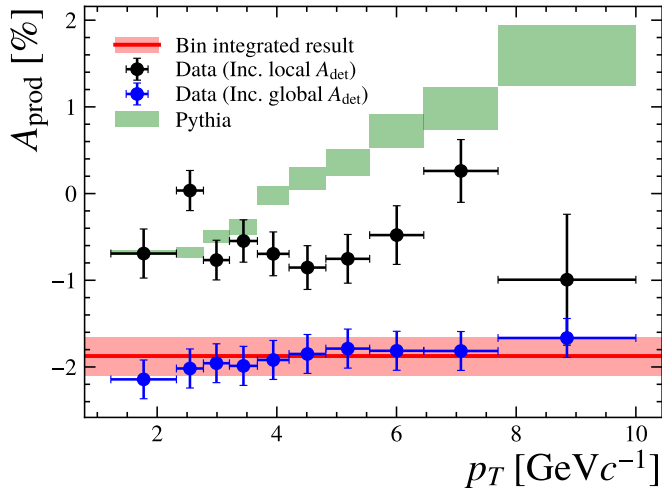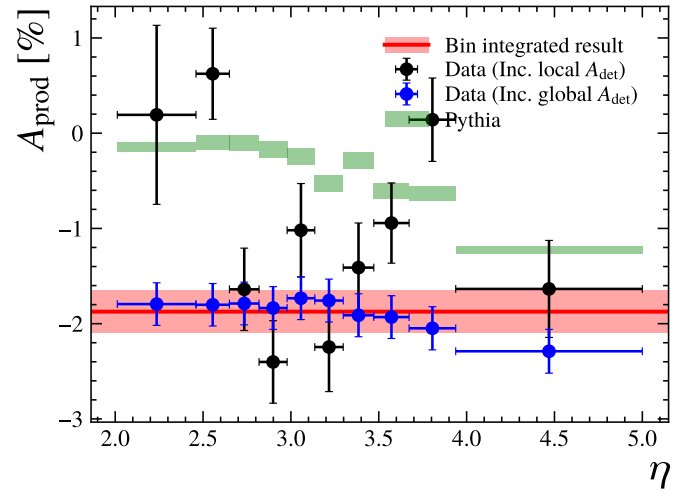

(a) 17 p_T

(b) 17 η
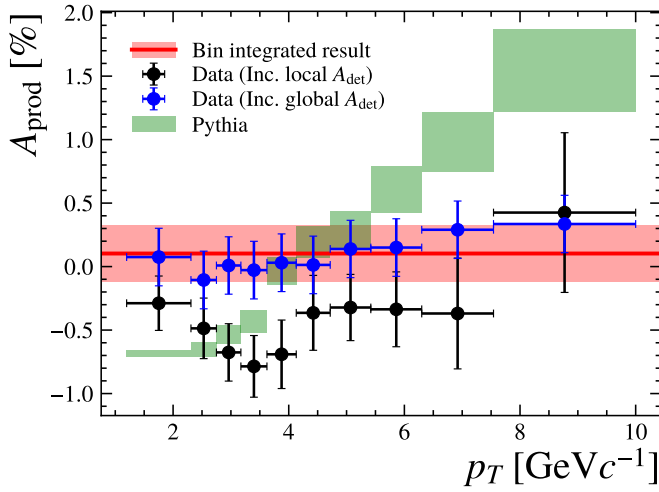
Fig. 29. Graphs showing the production asymmetry in each phase-space bin. The value for the kinematic variable is found by calculating the bin centre, and its error is half the bin width.

(a) 18 p_T

(b) 18 η

Fig. 30. Graphs showing the production asymmetry in each phase-space bin. The value for the kinematic variable is found by calculating the bin centre, and its error is half the bin width.